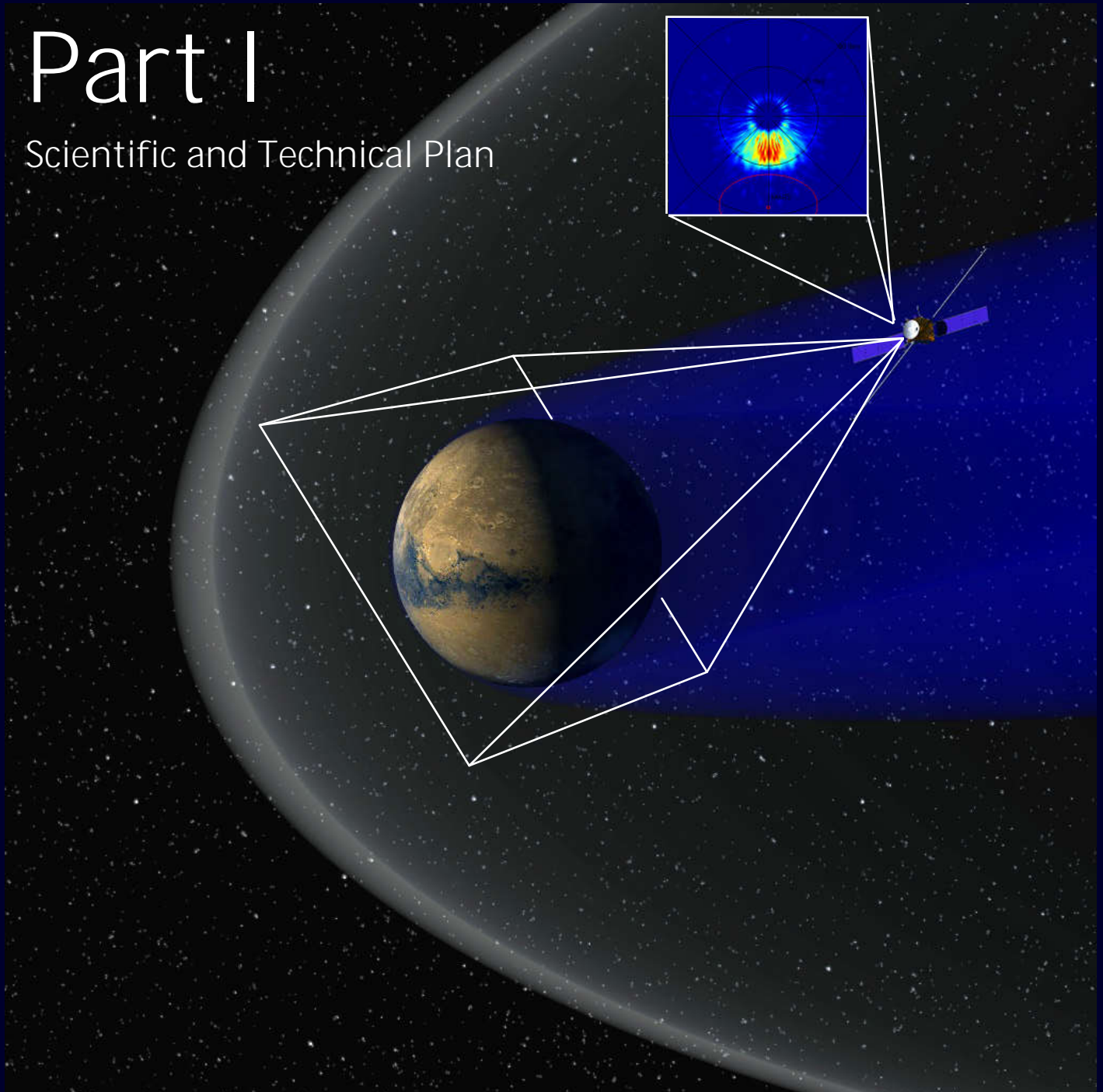


ASPERA-3

A proposal for an energetic neutral atom analyzer for the ESA Mars Express mission

Part I

Scientific and Technical Plan



Submitted by the
Swedish Institute of Space Physics, Kiruna
February 1998

This page is intentionally left blank.

ASPERA-3

Analyzer of Space Plasmas and Energetic Atoms

PRINCIPAL INVESTIGATOR

Rickard Lundin

Swedish Institute of Space Physics
Box 812, SE-981 28 Kiruna, Sweden
Phone: +46-980 79063
Fax: +46-980 79050
E-mail: rickard@irf.se

EXPERIMENT MANAGER

Joakim Gimholt

Swedish Institute of Space Physics
Phone: +46-980 79055
E-mail: jogi@irf.se

CO-INVESTIGATORS WITH HARDWARE RESPONSIBILITIES:

S. Barabash (Co-PI),

O. Norberg, M. Yamauchi

Swedish Institute of Space Physics, Kiruna (IRF)

H. Koskinen, E. Kallio

Finnish Meteorological Institute (FMI)
(Koskinen also at University of Helsinki, HU)

S. Livi, N. Krupp, J. Woch

Max-Planck-Institut für Aeronomie (MPAe)

S. Orsini, R. Cerulli-Irelli

Istituto di Fisica dello Spazio Interplanetari
(IFSI)

M. Grande

Rutherford Appleton Laboratory (RAL)

D. Winningham, J. Sharber, R. Frahm

Southwest Research Institute (SwRI)

J.-A. Sauvaud

Centre d'Etude Spatiale des Rayonnements (CESR)

THEORY CO-INVESTIGATORS:

E. Roelof, D. Williams

Applied Physics Laboratory (APL)

J. Luhmann

Space Science Laboratory (SSL)
University of California in Berkeley

J. Kozyra

Space Physics Research Laboratory (SPRL)
University of Michigan

K. C. Hsieh, B. R. Sandel, C. C. Curtis

University of Arizona (UA)

A. Fedorov

Space Research Institute, Moscow (IKI)

This page is intentionally left blank.

ASPERA-3

Analyzer of Space Plasmas and Energetic Atoms

Executive Summary

Principal Investigator: R. Lundin, Swedish Institute of Space Physics, Kiruna, Sweden

Scientific objectives: The general scientific objective of the ASPERA-3 experiment is to study the solar wind - atmosphere interaction and characterize the plasma and neutral gas environment in the near-Mars space through energetic neutral atom (ENA) imaging. The main scientific objectives can be subdivided into specific scientific tasks:

- Determine the instantaneous global distributions of plasma and neutral gas near the planet;
- Study plasma induced atmospheric escape;
- Investigate the modification of the atmosphere through ion bombardment;
- Investigate the energy deposition from the solar wind to the ionosphere;

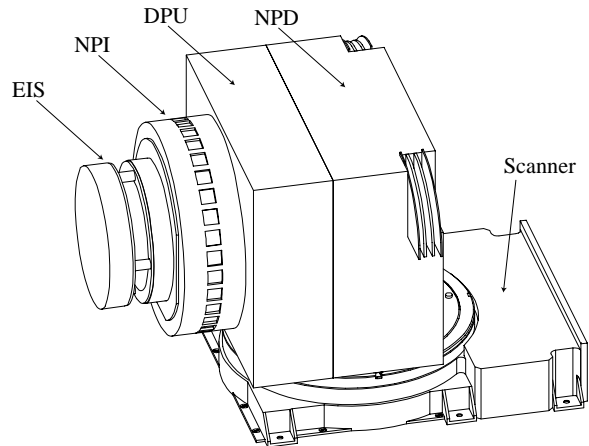
The studies to be performed address the fundamental question: *How strongly do the interplanetary plasma and electromagnetic fields affect the Martian atmosphere?* This question is directly related to the problem of Martian dehydration. Where is the Martian water? Is it lost or frozen and buried? If it is the former, what could produce such an effective escape mechanism? If the latter, where is this tremendous amount of water stored? Since liquid water is the fundamental requirement for life, a clear understanding of the fate of the Martian water is a crucial issue in resolving the problem *whether or not life existed on Mars in the past.*

No instrumentation with similar scientific objectives has or is planned to be flown to Mars.

Measurement principles and instrument performance: The ASPERA-3 instrument comprises three sensors; two ENA sensors and an electron and ion spectrometer. The two ENA sensors are optimized for some of the scientific objectives while at the same time complementing each other. This approach also gives the necessary redundancy.

The Neutral Particle Imager (NPI) provides measurements of the integral ENA flux with no mass and energy resolution but high angular resolution. The sensor utilizes reflection and ion sputtering from a graphite surface to detect ENAs and suppress the UV background. NPI is a replica of the ENA sensor used in the ASPERA-C experiment on the Mars-96 mission

and was successfully flown on the Swedish microsatellite Astrid, launched in 1995.



The Neutral Particle Detector (NPD) provides measurements of the ENA flux, resolving velocity and mass (H and O) with a coarse angular resolution. ENAs incident on a surface at a grazing angle of 20° are reflected and cause secondary electrons used for the START signal. The reflected ENAs hit the second surface and again produce secondary electrons utilized for the STOP signal. The time-of-flight (TOF) electronics give the ENA velocity. The pulse-height distribution of the START signal roughly determines the ENA mass. The NPD sensor is a new development.

The Electron and Ion Spectrometer (EIS) is a standard top-hat electrostatic analyzer in a very compact design. EIS is a replica of the MEDUSA experiment for the Astrid-2 and Munin missions to be launched in 1998 and 1999 respectively.

All three sensors are located on a scanning platform space qualified for the Mars-96 mission. The combination of the 360° field of view and the scans from 0° to 180° give the 4π maximum coverage. Mechanically the instrument is one unit.

In the *optional configuration* the instrument is complemented by a mass resolving sensor, IMA (Ion Mass Analyzer) and the EIS sensor is reduced to an electron spectrometer. Mechanically IMA is a separate unit connected by a cable to the ASPERA-3 experiment.

IMA provides ion measurements in the energy range 0.001 - 40 keV/q for the main ion components H⁺, H₂⁺, He⁺, O⁺, the group of molecular ions (20 - 80 amu/q), and up to 10⁶ amu/q (dusty plasma). The instantaneous field of view is 4.6°×360°. The elevation (±45°) coverage is performed by electrostatic sweeping. The IMA sensor is a spherical electrostatic

analyzer followed by a circular magnetic separating section. A large diameter MCP with a discrete anode images azimuth × mass. The G-factor per pixel is 3.5×10⁻⁴ cm²sr. IMA is a copy of the Ion Composition Analyzer (ICA) for the ESA Rosetta mission.

The baseline instrument performance

	NPI	NPD	EIS
Particles to be measured	Neutrals	Neutrals	Ions and Electrons
Energy range, keV	≈0.1 - 60	0.1 - 10	0.001 - 20
Energy resolution, steps	No	16	32 (e ⁻), 96 (ions)
Mass resolution,	No	H, O	No
Intrinsic field of view	9° × 344°	9° × 180°	10° × 360°
Angular resolution (FWHM)	4.6° × 11.5°	5° × 30°	10° × 22.5°
G-factor/pixel (ε not included), cm ² sr	2.5 × 10 ⁻³	6.2 × 10 ⁻³	3×10 ⁻⁴ (e ⁻), 1×10 ⁻⁴ (ions)
Time resolution for full 3D, s	32	32	32

Required spacecraft resources

Parameter	Baseline	Optional design
Mass, kg	5.95	7.85
Power, W	6.4	9.3
Dimensions, mm (including rotation)	379 × 433 × 234	359 × 393 × 234 (main unit) 255 × 150 × 150 (IMA)
Telemetry, Mbyte / orbit	2, 7, 20	2, 7, 20

Management scheme: To fabricate, test, operate the instrument, and analyze the data to be received we have assembled a strong team of scientists and engineers with wide experience in space instrumentation and, in particular, in ENA imaging and physics of the solar wind interaction with the non-magnetized planets Mars and Venus. The team will be led by the Principal Investigator, who assumes full responsibility for the final assembly and delivery for the instrument package. The responsibilities within the team are listed below.

- Swedish Institute of Space Physics, Kiruna: PI institute, NPI, NPD, EIS, IMA, scanner;
- Finnish Meteorological Institute, Helsinki: DPU;
- Southwest Research Institute, San Antonio: EIS;
- Max-Planck-Institut für Aeronomie, Lindau: TOF electronics for the NPD;
- Rutherford Appleton Laboratory: MCP assemblies for the NPD;

- Istituto di Fisica dello Spazio Interplanetari, Rome: EGSE, mechanical and electronic support;
- Centre d'Etude Spatiale des Rayonnements, Toulouse: Electronic support;
- Theoretical support - Applied Physics Laboratory, Laurel; Space Physics Research Laboratory, University of Michigan; Space Research Institute, Moscow; Space Science Laboratory, University of California in Berkeley; University of Arizona, Tucson.

Funding status: The participating institutions have submitted or will submit funding requests to their national funding agencies. NASA funding will be requested but is not required for the instrument development, science operation and scientific analysis.

Departures from constraints stated in the AO: To fulfill the requirements listed in the Payload Definition Document the instrument mass increased 950 g and the power consumption 0.4 W in comparison to the ones listed in the AO.

Part I: SCIENTIFIC AND TECHNICAL PLAN

Table of Contents

1. Scientific objectives and instrument capabilities.....	1
1.1 Introduction. Plasma and neutral environments of Mars.....	1
1.3 The solar wind - atmosphere coupling.....	2
1.2 Sources of energetic atoms at Mars.....	4
1.4 ENA imaging of the Martian environment.....	6
1.5 Scientific objectives and measurements requirements.....	7
1.6 Measurement principles and instrument capabilities.....	7
1.7 Design option.....	9
1.8 Expected results.....	10
1.9 Extracting diagnostic using ENA images.....	13
2. Proposed investigation in context of other missions.....	15
3. Technical description.....	15
3.1 Overview.....	15
3.2 Neutral Particle Imager. NPI.....	16
3.3 Neutral Particle Detector. NPD.....	18
3.4 Electron and Ion Spectrometer. EIS.....	23
3.5 Ion Mass Analyzer. IMA (design option).....	24
3.6 EElectron Spectrometer (design option).....	26
3.7 Scanner.....	26
3.8 Digital Processing Unit. DPU.....	27
3.9 Operating and TM modes.....	28
3.9.1 Operating modes and time resolutions.....	28
3.9.2 Raw data and TM modes.....	28
3.10 Instrument accommodation on the spacecraft.....	29
3.11 System reliability and redundancy.....	29
4. Data reduction and scientific analysis plans.....	30
5. Test and calibration plan.....	31
6. System level assembly, integration and verification.....	32
7. Flight operations.....	33
8. Organization and management structure of the instrument team.....	33
8.1 Instrument development.....	33
8.2 Science operations.....	34
9. Description of the instrument team qualifications and experience.....	35
9.1 Scientific personnel.....	35
9.2 Key technical personnel.....	37
9.3 Relevant publications.....	38
References.....	39

This page is intentionally left blank.

1. Scientific Objectives and Instrument Capabilities

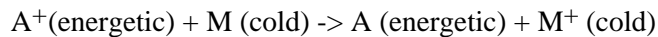
The scientific objectives of the Mars Express Orbiter mission are to study the subsurface, the surface, and the atmosphere of Mars, as well as the interaction of the atmosphere with the interplanetary medium. To fulfill the last scientific objective we propose the experiment ASPERA-3 (Analyzer of Space Plasma and Energetic Atoms) which will perform:

(1) remote measurements of energetic neutral atoms (ENA) in order to (a) investigate the interaction between the solar wind and Martian atmosphere, (b) characterize quantitatively the impact of the plasma process on the atmosphere evolution, and (c) obtain the global plasma and neutral gas distributions in the near - Mars environment,

(2) in situ measurements of ions and electrons in order to (a) complement the ENA images (electrons and multiply-charged ions cannot be so imaged) (b) provide undisturbed solar wind parameters necessary for interpretation of ENA images.

1.1 Introduction. Plasma and Neutral Environments of Mars

As was established by earlier missions and confirmed recently by the Mars Surveyor [*Acuna et al.*, 1997], Mars possesses a very weak, intrinsic dipole core magnetic field. The field only starts playing a role in the solar wind interaction during periods of the high dynamic pressure while for the normal conditions the solar wind interacts directly with the Martian ionosphere and upper atmosphere / exosphere. Furthermore, as a result of the low gravity on Mars, the neutral density can reach $10^4 - 10^6 \text{ cm}^{-3}$ in the interaction region where the main plasma boundaries, the bow shock and the magnetopause are located. The co-existence of these two components, the solar wind plasma and the planetary neutral gas, results in a strong interaction between them. One of the fundamental collisional interactions is the charge - exchange process



which produces energetic neutral atoms (ENA). Directional detection of the ENA thereby yields a global image of the interaction. The ASPERA-3 experiment will concentrate on studying the effects of the plasma - neutral coupling at Mars via ENA imaging, complemented by the electron and ion observations.

The basic plasma boundaries, such as the bow shock and magnetopause (at Mars, the boundary where the solar wind proton flux disappears), and the plasma tail were discovered by the first missions to the planet, Mars 2, 3, and 5 and Mariner 6 and 7 (*Vaisberg*, 1976). Phobos-2 substantially expanded our knowledge of the Martian plasma environment by carrying out detailed investigations of particles, fields and waves. The ASPERA/PHOBOS experiment during which the first 3D plasma composition investigations were conducted near Mars, showed that the Martian magnetosphere was dominated by ions of Martian origin, namely, O^+ and molecular ions, and established the importance of plasma - induced escape for atmospheric evolution (*Lundin et al.*, 1989, *Lundin et al.*, 1990). The ASPERA observations resulted in the general view of the Martian plasma environment depicted in Figure 1.1.1.

Most of what we know about the neutral atmosphere below the exobase (~200 km on Mars) has come from the Viking mission landers (see review by *Luhmann and Brace*, 1991). Very few measurements of the neutral gas distribution at higher altitudes are available. The Lyman α measurements onboard Mariner 6, 7 (*Anderson*, 1974) and Mars 2,3 (*Dostovalov and Chuvahin*, 1973) were used to obtain the hydrogen density profile up to 20000 km. The EUVE (Extreme Ultraviolet Explorer) measurements of the He 58.4 nm airglow were used by *Krasnopolsky and Gladstone* (1996) to reconstruct the helium profile. The measured distribution of the planetary H^+

and He^+ pick-up ions along the PHOBOS orbit was also used to obtain profiles of these components (Barabash *et al.*, 1991; Barabash *et al.*, 1995a). The hot oxygen corona formed via electron dissociative recombination (Nagy and Cravens, 1988; Ip, 1988) is one of the most interesting and important features of the Martian neutral environment. Since the corona extends much above the obstacle boundary, the corona atoms and molecules being ionized are picked up by the flowing plasma and can effectively escape the planet. Figure 1.1.2 shows the profiles of the main neutral components which can interact with the solar wind plasma. Curves for H, H_2 , and He were adopted from Krasnopolsky and Gladstone (1996) and that for oxygen from Zhang *et al.* (1993). All profiles are sensitive to the solar EUV flux and shown for the solar maximum conditions. We have also marked the sub-solar altitudes of the main plasma boundaries to show that the neutral gas density is high in the principal magnetospheric domains; this results in the strong plasma - atmospheric coupling.

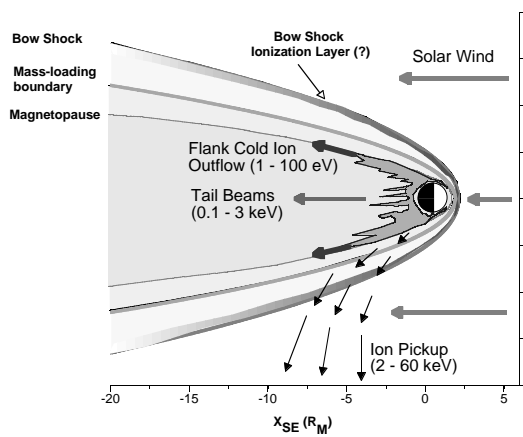


Figure 1.1.1. General view of the Martian plasma environment based on the ASPERA / Phobos observations.

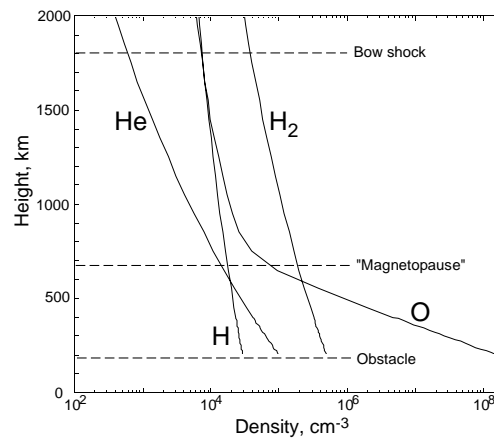


Figure 1.1.2. The main components of the Martian exosphere. The altitudes of the principal plasma domains are marked.

1.2 The Solar Wind - Atmosphere Coupling

Near-Mars space is strikingly different from Earth-space because of the absence of a substantial intrinsic magnetic field of Mars. Without the magnetic cavity of a magnetosphere to shield the upper atmosphere from the on-coming solar wind, Mars is subject to comet-like atmosphere erosion processes and solar-wind-induced current systems that have no terrestrial counterparts. From both previous missions to Mars (especially the Phobos-2 mission) and experience gained in orbit around similarly weakly magnetized Venus on the Pioneer Venus Orbiter, we have developed ideas of how the Mars upper atmosphere and solar wind interact and the consequences for the planet. In particular, we have observed that the scavenging of planetary ions may have resulted in the removal of ~1 m of surface water over 4.5 billion years (Lundin *et al.*, 1991). More detailed studies [Perez-de-Tejada, 1992], which take into account the variability of the ionosphere through planetary history, give a much higher (~30 m) equivalent depth of water which has escaped due to the solar wind interaction process.

The current atmospheric conditions on Mars indicate that water does not exist on the surface in any significant amount (an equivalent water layer is 15 μm deep [Farmer *et al.*, 1977]). On the other hand, water associated with active volcanism existed in the past on the Martian surface. The total amount of water released in the past together with volcanic material identified on the surface resulted in an equivalent water layer of 50 - 80 m. Thus we come to the problem of Mars dehydration. Where is the Martian water? Is it lost or frozen and buried? If it is the former, what could produce such an effective escape mechanism? If the latter, where is this tremendous amount of water stored? As

indicated above, the processes associated with the solar-wind interaction could account for the escape of at least half the amount of water delivered to the Martian atmosphere through early volcanic activity.

The solar wind can not only cause erosion of the neutral environment but it can also deposit matter in the Martian atmosphere as well. From analyzing the data on the helium non-thermal escape from Mars, *Barabash et al.* [1995a] suggested that helium may be delivered to the Martian atmosphere as solar wind α particles. Indeed, the hybrid simulation of the solar wind - Mars interaction has recently revealed that the solar wind ions can reach the Martian ionosphere due to their large gyro-radius in comparison with the thickness of interaction region (*Brecht, 1997*). Depending on the interplanetary magnetic field conditions, the He delivery can be three times higher than the estimated internal production. This illustrates how important the solar wind may be for the evolution of certain atmospheric components.

Another problem of the solar wind - atmosphere coupling that has not been explored experimentally concerns the energetic consequences for the Martian atmosphere of the lack of a Martian dipole field of importance. Recent models of the Mars-solar wind interaction (*Brecht, 1997*; *Kallio et al., 1997*) have suggested that solar wind absorption by the Martian atmosphere may be an important energy source for the upper atmosphere. The ENAs generated as a product of the solar - wind interaction enhance the deposition of solar wind flux and, at the same time, provide a means of "imaging" the solar wind interaction. The Martian atmosphere, although thin, alters the incoming energetic solar wind by (a) generation of ionospheric currents that partially deflect the ion flow around the Martian ionosphere, (b) "mass loading" the solar wind with planetary ions produced mainly by photoionization, and solar wind electron impact ionization of the atmospheric gases, and (c) undergoing charge-transfer or charge-exchange interactions with the solar wind ions. According to the models, some of the solar wind ions (mainly protons and alphas) directly impact Mars' upper atmosphere near its exobase (at ~ 180 km altitude) because their gyroradii are too large to behave as a deflected "fluid" in the subsolar magnetosheath (see *Brecht, 1997*) or because they are partially thermalized by the bow shock (*Kallio et al., 1997*). Others undergo charge exchange reactions with ambient exospheric and thermospheric neutrals, particularly hydrogen and helium and then impact the exobase as ENAs (*Kallio et al., 1997*). In both cases, solar wind energy is "directly" deposited into the upper atmosphere. Figure 1.2.1 taken from *Kallio et al., (1997)* shows the relative importance of different heat sources in the Martian ionosphere. The first and second bars show the total heating due to the radiation absorption and the heat deposited as kinetic energy of ions. The third and fourth bars show the ENA precipitating energy deposited onto the upper atmosphere. The fifth and the sixth bars indicate the energy flux supplied by precipitating O^+ and H^+ ions.

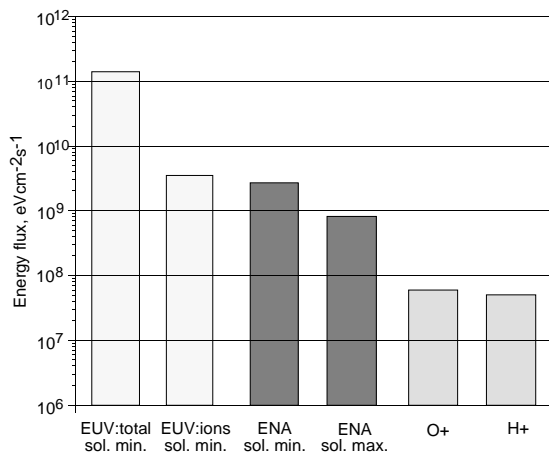


Figure 1.2.1. *The relative importance of different heat sources in the Martian ionosphere.*

Around the Earth, "space weather" is dominated by the magnetosphere's particle populations and by their response to solar wind conditions. When solar eruptions in the form of Coronal Mass Ejections (CMEs) occur, they may launch large, high speed ejecta into interplanetary space that compress the solar wind around them. During the decline of solar activity (when Mars Express will be in orbit), there are also 26-day recurrent Corotating Interaction Regions (CIRs) in the solar wind whose compressions in density and magnetic field also trigger modifications in planetary magnetospheres. When these disturbances reach the Earth, they compress the magnetosphere and drive the injection of "ring

currents" of particles that cause significant alterations in the Earth's surrounding magnetic field and considerably disturb the stability of the radiation belts. These magnetic storm-time ring currents subsequently decay in large part by charge exchange of the ring current ions with the hydrogen geocorona atoms in a process that produces both observable ENA fluxes (e.g. *Roelof, 1987; Henderson et al., 1997*) and aeronomical consequences (*Kozyra, 1992; Bauske et al., 1997*). From these perspectives the question arises; How does the Martian space weather affect the atmosphere? When CMEs or CIRs pass Mars, the solar wind disturbances must directly impact the atmosphere thereby compounding any effects from associated energetic (e.g. XUV) photon or particle ionospheric enhancements. Essentially nothing is known about the details of the "magnetic storm" counterpart on a weakly magnetized planet with a thin atmosphere like Mars. From the aeronomical picture described above, we can speculate that the direct solar wind absorption may decrease because the increase in the interplanetary magnetic field will make the proton gyroradii smaller. The charge exchange rate could, however, greatly increase if the solar wind is compressed at the edges of the CMEs and CIRs. In addition to increasing the energy deposition in the upper atmosphere by the ENAs, CMEs and CIRs may literally "light up" Mars in ENAs as they pass. Thus ENA measurements made by the Mars Express will provide unique and important information for the aeronomical study of Mars, as well as a visual impression of near-Mars space-weather.

1.3 Sources of Energetic Neutral Atoms at Mars

The ENA production at Mars was considered by *Barabash et al. (1995b)* and *Kallio et al. (1997)*. ENAs are produced by charge - exchange between the Martian exosphere containing H, H₂, He and O, and the different plasma populations such as (1) the supersonic solar wind, (2) the shocked solar wind, and (3) accelerated planetary ions. The tiny Phobos atmosphere (4) can also interact with both the supersonic and the shocked solar wind resulting in ENA generation. The heavy planetary O⁺ ions picked up by the plasma flow can re-enter the atmosphere causing effective sputtering of oxygen (*Luhmann and Kozyra, 1991*). The back-scattered atoms have energies up to few hundred eV and form the ENA albedo (5) . With the ASPERA-3 experiment we are going to study all of these ENA sources and search for new ones.

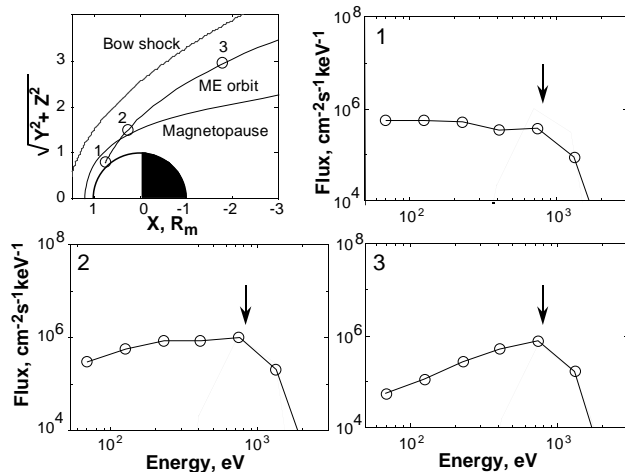


Figure 1.3.1. ENA spectra along the Mars Express orbit. The ENAs originate in the shocked solar wind. The arrows mark ENA flux produced in the upstream solar wind. The energy resolution corresponds to that for ASPERA-3.

these models we simulated ENA images that would be observed from the Mars Express orbit for the solar maximum conditions. The spacecraft will actually reach Mars during the moderate solar activity characteristic of the decline of the solar cycle, but the ENA emissions are weaker during the solar maximum and our calculations give, thus, the lower limits for the ENA fluxes. Figure 1.3.1

shows the ENA spectra integrated over the unit sphere for several locations along the Mars Express orbit. The estimated ENA fluxes are well above $10^4 \text{ cm}^{-2}\text{s}^{-1}\text{keV}^{-1}$ and therefore easily detectable.

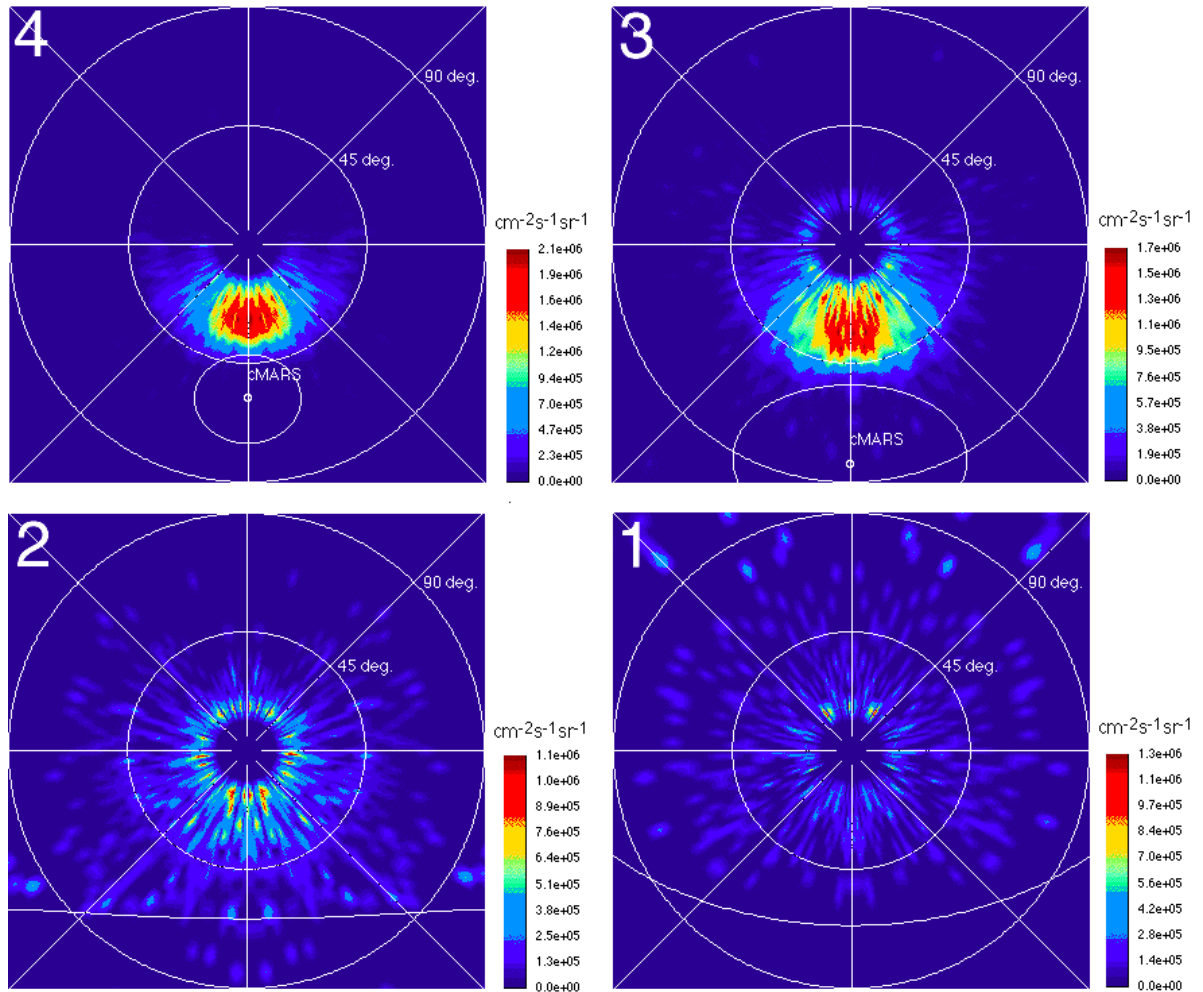


Figure 1.3.2. ENA images for four locations along the Mars Express orbit marked in the inset of Figure 1.3.1. The position 4 not shown in Figure 1.3.1 corresponds to the orbit apoapsis. The polar axis is looking toward the Sun. The solar wind ENAs are blocked.

Figure 1.3.2 shows the directional ENA flux integrated over energy as a function of two spherical angles (ENA images) for the same positions. In this projection, the polar axis is looking toward the Sun. The images simulated for the four locations along the Mars Express orbit marked in the inset of Figure 1.3.1 display the entire interaction region and can be converted into global distributions of the proton flow and neutral gas using the extracting diagnostic methods described in Section 1.9. The directional fluxes to be measured well exceed $10^5 \text{ cm}^{-2}\text{s}^{-1}\text{sr}^{-1}$.

Some of the ENAs produced by the shocked solar wind as well as ENAs originated in the solar wind can precipitate onto the Martian ionosphere (Section 1.2). Figure 1.3.1 (position 1 inside the magnetosphere) gives a typical spectrum of precipitating ENAs at the 45° solar zenith angle. The spectrum is rather flat at the level $7 \cdot 10^6 \text{ cm}^{-2}\text{s}^{-1}\text{keV}^{-1}$. The peak corresponds to the solar wind energy.

The ASPERA / PHOBOS observations of the plasma energization inside the Martian magnetosphere (Lundin *et al.*, 1993) have shown the existence of two basic ion populations, the tail beams of H^+ and O^+ with energy 1-3 keV and outflowing ionospheric ions with energy 0.1 - 100 eV near the tail flanks. Barabash *et al.* (1995b) estimated the related ENA flux to be $10^3 \text{ cm}^{-2}\text{s}^{-1}\text{keV}^{-1}$

for the energy range 1 - 10 keV, and up to $10^5 \text{ cm}^{-2}\text{s}^{-1}\text{keV}^{-1}$ for the lower energies 10 - 100 eV. ENA

Several experiments on the PHOBOS mission observed brief plasma disturbances when the spacecraft crossed the Phobos orbit (see review and references by *Barabash*, 1996c). They could be

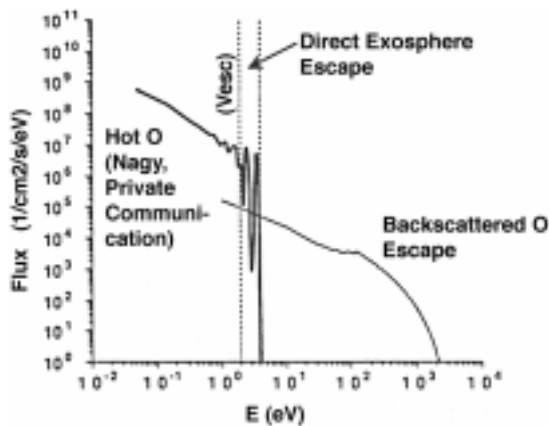


Figure 1.3.3. Calculated flux of the back-scattered oxygen (*Luhmann and Kozyra*, 1991).

related to a hypothetical neutral gas torus resulting from the moon outgassing. The solar wind plasma can experience charge - exchange with the Phobos "atmosphere" and the neutral torus resulting in ENA emissions. *Barabash et al.* (1995) estimated the Phobos ENA flux to be of the order of $10^4 - 10^6 \text{ cm}^{-2}\text{s}^{-1}$. Due to solar radiation, the Phobos ENAs and the Phobos torus ENAs can only be observed when the moon is in the magnetosheath and the plasma flow deviates strongly from the anti-solar direction.

The energetic pick-up O^+ ions incident on the atmosphere sputter or back-scatter oxygen, CO_2 and its fragments (*Luhmann and Kozyra*, 1991; *Luhmann et al.*, 1992). Figure 1.3.3 shows the energy spectrum of the back-scattered oxygen.

1.4 ENA Imaging of the Martian Environment

With the ASPERA-3 experiment we will image all of the above ENA sources. ENA images to be obtained provide twofold information. First of all, they reveal morphological features of the ENA sources such as the location of boundaries and the relative sizes. ENA images are useful, in particular, for investigating different types of asymmetries expected for the plasma flow near Mars (*Dubinin et al.*, 1996).

The ENA images of the escaping plasma display globally and instantaneously the size and geometry of the outflowing plasma region. These characteristics are particularly important for calculations of the total non-thermal plasma outflow. For instance, the local ion measurements made using two instruments, ASPERA and TAUS, during the PHOBOS mission gave comparable ion fluxes. However, different assumptions made regarding the outflow region geometry (mass - loading boundary, plasma sheet) resulted in significant differences in the total outflow rate estimations, 0.5 - 1.0 kg/s (*Lundin et al.*, 1989) and 0.15 kg/s (*Verigin et al.*, 1991). One of the reasons for this was ambiguity in separating spatial and temporal variations which is typical for local plasma measurements. Global and instantaneous observations of the outflowing plasma region morphology to be made via ENA imaging would help to resolve this issue which is important for understanding the planetary atmosphere evolution (Section 1.2).

Beside morphological features, ENA images carry an ample amount of the quantitative information about both the planetary plasma and neutral environments. By applying the extraction techniques described in Section 1.9 to the images of the shocked solar wind, we plan to obtain the quantitative models giving the neutral gas profiles, namely, the exobase densities and temperatures, and global proton plasma distributions, namely, the flow geometry, bulk velocity, density, and temperature.

Recent aerobraking measurements from the Mars Global Surveyor (*Dornheim*, 1997) indicate that the atmospheric density at 150 km altitude can vary by 30% in one out three passes. Estimated scale heights of $\sim 8 \text{ km}$ implies that the densities in the interaction region higher up will also be much more variable with time than had been expected. Global ENA imaging of the interaction offers the greatest promise of separating the spatial and temporal variations of the atmosphere - solar wind interaction.

Apart from imaging, the measurements of ENA flux from certain directions is a powerful tool in plasma - atmosphere coupling studies. Precipitating ENAs and ENA albedo (back-scattered oxygen) are direct manifestation of such an interaction. We plan to perform a comprehensive study of these phenomena.

1.5 Scientific Objectives and Measurements Requirements

The studies of Martian ENAs resulting from the solar wind - atmosphere interaction address the fundamental question: **How strongly do the interplanetary plasma and electromagnetic fields affect the Martian atmosphere?** This question is directly related to the problem of Martian dehydration as described in Section 1.2. **What happened to the Martian water** which once flowed in numerous channels? As we know from our earth's experience, together with an inventory of organic compounds and external energy sources, liquid water is a fundamental requirement for life. Therefore, a clear understanding of the fate of the Martian water is a crucial issue in resolving the problem **whether or not life existed on Mars in the past.**

The general scientific task, to study the solar wind - atmosphere interaction through ENA imaging, can be subdivided into specific scientific objectives, these are listed in Table 1.5.1 together with the corresponding instrument requirements.

Table 1.5.1. The ASPERA-3 scientific objectives

Scientific objectives	Associated measurements	Measurements requirements
Determine the instantaneous global distributions of plasma and neutral gas near the planet	ENAs originated from the shocked solar wind	Measure the ENA flux in the energy range tens eV - few keV with 4π coverage. ENA flux $> 10^4 \text{ cm}^{-2}\text{s}^{-1}\text{keV}^{-1}$ Measure the upstream solar wind parameters
Study plasma induced atmospheric escape	ENAs originated inside the magnetosphere	Mass resolving (H / O) ENA measurements in the energy range up to tens keV. ENA flux $> 10^3 \text{ cm}^{-2}\text{s}^{-1}\text{keV}^{-1}$
Investigate the modification of the atmosphere through ion bombardment	ENA albedo	Mass resolving (H / O) ENA measurements in the energy range down to tens eV from the nadir direction ENA flux $> 10^6 \text{ cm}^{-2}\text{s}^{-1}\text{keV}^{-1}$ (100 eV)
Investigate the energy deposition from the solar wind to the ionosphere	Precipitating ENAs	ENA measurements in the energy range tens eV - few keV. ENA flux $> 10^4 \text{ cm}^{-2}\text{s}^{-1}\text{keV}^{-1}$
Search for the solar wind - Phobos interactions	ENA originated from Phobos	ENA measurements in the energy range tens eV - few keV with 4π coverage ENA flux $10^4 \text{ cm}^{-2}\text{s}^{-1}\text{keV}^{-1}$
Define the local characteristics of the main plasma regions	Ions and electron measurements of hot plasma	Ion and electron measurements in the energy range few eV - tens keV with 4π coverage

1.6 Measurement Principles and Instrument Capabilities

To fulfill the scientific objectives listed above the ASPERA-3 instrument comprises three sensors; two ENA sensors and an electron and ion spectrometer. The two ENA sensors are optimized for some of the scientific objectives while at the same time complementing each other. This approach also gives the necessary redundancy as well as independent cross-checking, necessary for such a

”first ever” measurements. The charged particle sensors not only provide characterization of the local plasma environment but support ENA measurements in terms of charged particles background and inter - calibrations. One of the ENA sensors can also provide ion velocity measurements; by combining these with the ion energy data one can roughly estimate the ion mass.

The Neutral Particle Imager (NPI) provides measurements of the integral ENA flux with no mass and energy resolution but with $5^\circ \times 11^\circ$ angular resolution. The intrinsic field of view is $9^\circ \times 344^\circ$. The sensor utilizes a graphite surface to suppress the UV background. ENAs incident on the surface at a grazing angle of 20° are reflected and / or cause ion sputtering. The reflected particles and sputtered fragments are detected by an MCP stack with a discrete anode. The NPI head is a replica of the NPI - MCP sensor developed for the ASPERA - C experiment on the Mars - 96 mission (launch failure) and successfully flown on the Swedish microsatellite Astrid launched in 1995.

The Neutral Particle Detector (NPD) provides measurements of the ENA differential flux over the energy range 100 eV - 10 keV resolving H and O with a coarse $5^\circ \times 30^\circ$ angular resolution. The sensor consists of two identical detectors each with a $9^\circ \times 90^\circ$ intrinsic field of view. The measurement technique is based on a principle similar to NPI. ENAs incident on a surface at a grazing angle of 20° are reflected and cause secondary electron emission. The secondary electrons are transported to an MCP assembly which gives the START signal. The reflected ENAs hit the second surface and again produce the secondary electrons used to generate the STOP signal. The time-of-flight (TOF) electronics give the ENA velocity. The pulse - height distribution analysis of the START signal is used to provide a rough determination of the ENA mass.

The Electron and Ion Spectrometer (EIS) provides electron and ion measurements in the energy range 0.001 - 20 keV. The intrinsic field of view is $10^\circ \times 360^\circ$. There are 16 fields of view each with 22.5° resolution. The sensor is a standard top - hat electrostatic analyzer in a very compact design. EIS is a replica of the MEDUSA experiment for the Astrid-2 and Munin missions to be launched in 1998, 1999.

All three sensors are located on a scanning platform. The combination of the 360° field of view and the scans from 0° to 180° give the required 4π maximum coverage (the real coverage depends on the instrument location on the spacecraft). Mechanically the instrument is one unit. Table 1.6.1 summarizes the baseline instrument performance. Table 1.6.2 specifies the scientific tasks for each sensor.

Table 1.6.1. The baseline instrument performance

	NPI	NPD	EIS
Particles to be measured	Neutrals	Neutrals	Ions and Electrons
Energy range, keV	$\approx 0.1 - 60$	0.1 - 10	0.001 - 20
Energy resolution, steps	No	16	32 (e^-), 96 (ions)
Mass resolution,	No	H, O	No
Intrinsic field of view	$9^\circ \times 344^\circ$	$9^\circ \times 180^\circ$	$10^\circ \times 360^\circ$
Angular resolution (FWHM)	$4.6^\circ \times 11.5^\circ$	$5^\circ \times 30^\circ$	$10^\circ \times 22.5^\circ$
G-factor / pixel, cm^2sr (efficiency not included)	2.5×10^{-3}	6.2×10^{-3}	3×10^{-4} (electrons) 1×10^{-4} (ions)
Time resolution for full 3D, s	32	32	32

The baseline instrument performance outlined in Table 1.6.1 corresponds to the one specified in Payload Definition Document (Section 1.5 Energetic Neutral Atoms Analyzer) for the electron spectrometer and differs slightly for the ENA imagers. The scientific justification and technical constraints resulting in the deviations in the energy range and angular resolution of the ENA sensors is explained below. No separate ion mass resolving sensor was included in the basic configuration due to the mass constraint factors. The configuration with an ion mass spectrometer is proposed as a design option.

Table 1.6.2. The measurement tasks

Scientific task	Primary sensor	Complementary sensors
Global plasma and neutral distributions	NPI, EIS	NPD
ENAs from the magnetosphere (escaping plasma)	NPD	NPI
ENAs precipitation	NPI	NPD
ENAs albedo	NPD	
Satellite interactions	NPI	NPD
Local 3D plasma characteristics and atmospheric escape	EIS	NPD

The energy range for ENAs was reduced and the low energy threshold lowered down to 100 eV. Mars does not possess a significant intrinsic magnetic field and, hence, cannot trap energetic charged particles. Indeed, the survey of the energetic (> 34 keV) ion population during the PHOBOS mission revealed comparatively weak fluxes in four regions: the subsolar magnetosphere; the terminator bow shock and magnetosheath; and the magnetotail (*McKenna-Lawlor et al.*, 1993). As shown by *Barabash et al.* (1995b) the corresponding ENA fluxes are low, typically, less than $5 \text{ cm}^{-2} \text{ s}^{-1} \text{ sr}^{-1} \text{ keV}^{-1}$ (≈ 30 keV) and thus are hardly detectable. From the scientific point of view (Section 1.3), monitoring the lower energy plasma populations (such as the shocked solar wind) provides more important information about how the Martian plasma environment affects the upper atmosphere than does monitoring more energetic populations. Moreover, ENA imaging over the lower energy range (10's of eV to a few keV) is the only technique which allows a determination of the instantaneous global plasma and neutral gas distributions near the planet. Extending the NPD upper energy range above typical solar wind energies to 10 keV also permits one to study the acceleration process inside the magnetosphere via ENA imaging. The energy overlap with the EIS energy range is sufficient for the flight inter - calibrations.

The low energy range of ASPERA-3 determines the techniques for ENA detection. Taking into account (1) mass constraints, (2) volume constraints, (3) short development time, (4) availability of flight proven components, we decided to utilize the reflecting surfaces at grazing angles of incidence. Due to a wide angular spreading of the incident beams (see review by *Funsten et al.*, 1994) this technique alone does not permit a determination of the required angular resolution. A further collimating of the reflected beam will reduce the instrument geometrical factor and cause significant energy loss. The proposed approach with two separate sensors, NPI and NPD, for the angular and energy analysis, solves the problem. The $4.6^\circ \times 11.5^\circ$ NPI angular resolution is optimized for the instrument size and mass. A further reduction in the angular resolution would require an increase in aperture area which would violate the mass / size constraints.

1.7 Design Option

In its basic configuration, the ASPERA-3 instrument does not contain the ion mass resolving sensors because the main scientific objective of the experiment, to study solar wind - atmosphere interaction, can be fulfilled by an ENA instrument and a simple ion and electron spectrometer alone. Moreover, the very low mass budget (5 kg) allocated in Announcement of Opportunity for the ENA instrument does not allow a replacement of the ion spectrometer with the ion mass spectrometer. However, as was demonstrated by the ASPERA / PHOBOS experiment, the mass resolving measurements are very important in understanding the solar wind - planet interaction (*Lundin et al.*, 1989). The acceleration processes induced by this interaction effectively remove the ionospheric ions such as O^+ , O_2^+ , CO^+ and present a significant sink for the Martian atmosphere (Section 1.2). **Inclusion of an ion mass spectrometer dedicated to studies of the planetary ion outflow in the**

scientific payload would significantly increase the scientific return from the Mars Express mission. The ENA measurements providing the global distributions of the plasma and neutral gas complemented by *in situ* measurements of the local plasma composition would supply very valuable information about the total non-thermal ion escape. In case the Mars Express mass budget does not permit including a stand-alone PI level mass spectrometer in the payload, **the ASPERA-3 experiment can be complemented by an ion mass resolving sensor.** This would however increase the mass of the instrument to 7.85 kg. The sensor in question is the Ion Mass Analyzer (IMA), an improved version of the ion mass spectrographs TICS / Freja, IMIS/Mars-96, IMI/Planet-B, and an exact copy of the ICA instrument to be flown on Rosetta mission. In this design option the IMA sensor is a separate unit connected by a cable to the ASPERA-3 experiment. The EIS sensor is replaced with Electron Spectrometer (ELS) to perform electron measurements only.

IMA provides ion measurements in the energy range 0.001 - 40 keV/Q for the main ion components H^+ , H_2^+ , He^+ , O^+ , the group of molecular ions ($20 < M/q < \sim 80$), and up to 10^6 amu/q. Mechanically the IMA is a separate unit with a $4.6^\circ \times 360^\circ$ field of view. Elevation ($\pm 45^\circ$) coverage is performed by electrostatic sweeping. The IMA sensor is a spherical electrostatic analyzer followed by a circular magnetic separating section. A large diameter MCP with a discrete anode images matrix azimuth \times mass. IMA uses an open magnetic separating system and is therefore able to investigate the plasma component with very high M/q (up to 10^6 amu/q), i.e. corresponding to a dusty plasma.

Table 1.7.1 shows the baseline performance of the IMA and ELS sensors. The ELS characteristics correspond to the EIS parameters for the electron measurements.

Table 1.7.1. The baseline performance of the IMA and ELS sensors for the optional configuration

	IMA	ELS
Particles to measure	Ions	Electrons
Energy range, keV / q	0.001 - 40	0.001 - 20
Mass range, amu	$1-10^6$	N/A
Mass resolution, steps	32	N/A
Intrinsic field of view	$4.6^\circ \times 360^\circ$	$10^\circ \times 360^\circ$
G-factor / pixel, cm^2sr	3.5×10^{-4}	3×10^{-4}
Time resolution for full 3D, s	32	32

The capability of measuring the "dusty" plasma component is a unique feature of IMA. There are many reasons to believe that the plasma near Mars contains a significant amount of dust originated from the meteor bombardment of the Martian moons (*Banaszkiewicz and Ip, 1991; Juhasz et al. 1993*). This dust experiences a complicated interaction with the magnetospheric plasma that affects the dust dynamics via the electrodynamic forces (*Horanyi et al., 1990*) and mass distribution via electrostatic fragmentation (*Barabash and Lundin, 1994*). The ASPERA / PHOBOS data on the detection of the ultra -heavy ion components obtained when the PHOBOS spacecraft was close to the Phobos moon orbits (*Barabash and Lundin, 1994*) still needs additional confirmations.

In the optional configuration the ASPERA-3 instrument will be able to perform ENA imaging and fulfill all of the scientific objectives listed in Table 1.5.1. In addition, studies of the planetary ion outflow will be possible. This significantly increases the scientific return from the experiment.

1.8 Expected Results

The ASPERA-3 experiment presents a unique combination of charged and neutral particle sensors. This synergistic approach will provide completely new information about the plasma and neutral gas coupling near Mars. These observations are crucial for understanding the impact of the plasma process on the current energy and mass balance in the upper atmosphere / ionosphere and the planetary evolution during the Solar system history. The plasma measurements to be made will

further advance understanding the role of the upper atmosphere in the solar wind interaction with Mars. The ASPERA-3 experiment can be considered as an interdisciplinary experiment contributing both to planetology and space plasma physics.

ASPERA-3 will be the first-ever experiment to investigate the low energy neutrals at another planet, so there should be un-expected discoveries. Beside the main task of surveying the ENA population, the ASPERA-3 experiment will perform the 3D local plasma observations along the Mars Express orbit which crosses the main plasma regions of the Martian magnetosphere (Figure 1.8.1).

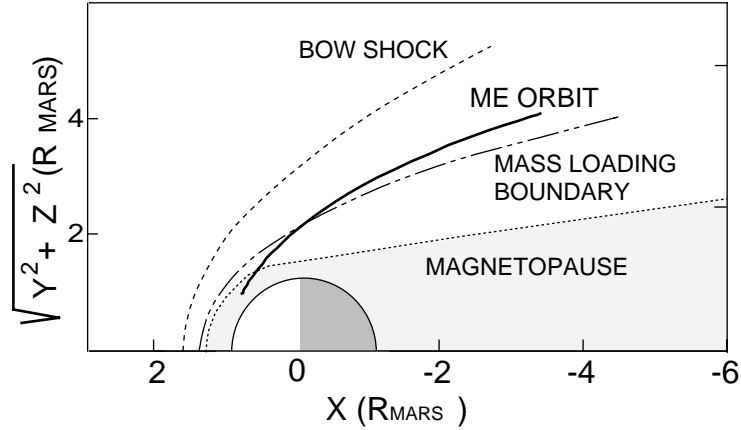


Figure 1.8.1. *The Mars Express orbit and the main domains of the Martian magnetosphere.*

ENAs carry information about both ion and neutral populations. Using the extracting diagnostics described in Section 1.9, the ENA images can be converted to corresponding global distributions, i.e., neutral gas profiles, and plasma density and bulk velocity distributions. Figure 1.8.2 shows, for example, the initial plasma flow field used to obtain ENA images in Figure 1.3.2. Such information will be extracted from the NPI and NPD images.

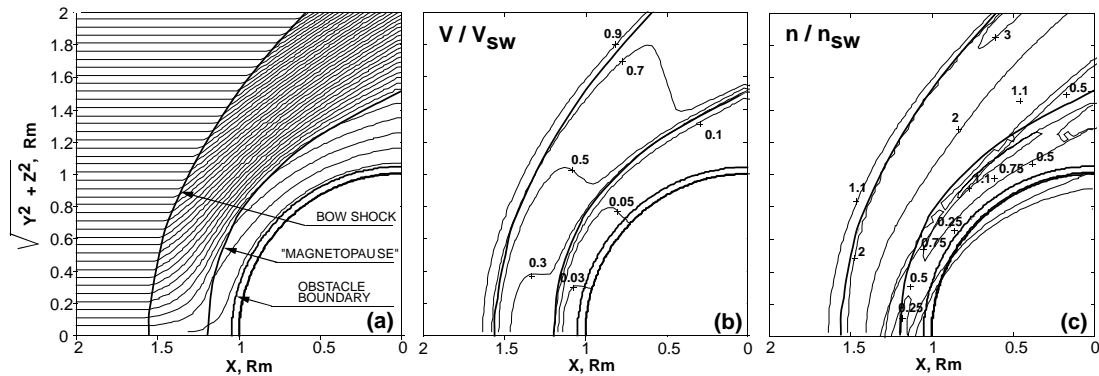


Figure 1.8.2. *The plasma distributions to be obtained from ENA images. The model is adapted from Kallio, 1996: (a) stream lines, (b) proton velocity, (c) proton density. All values are normalized to undisturbed solar wind values.*

To verify the instrument capabilities we converted the modelled ENA images (Figure 1.3.2) into ENA images to be seen by the NPI and NPD sensors from different points along the Mars Express orbit. The accumulation time was assumed to be 10 sec which corresponds to a 320 sec 0°-180° scan and an azimuth resolution of 6°. The counting statistic is the result of the Monte - Carlo method used in the simulation. The expected count rates are sufficient to adequately present the interaction region.

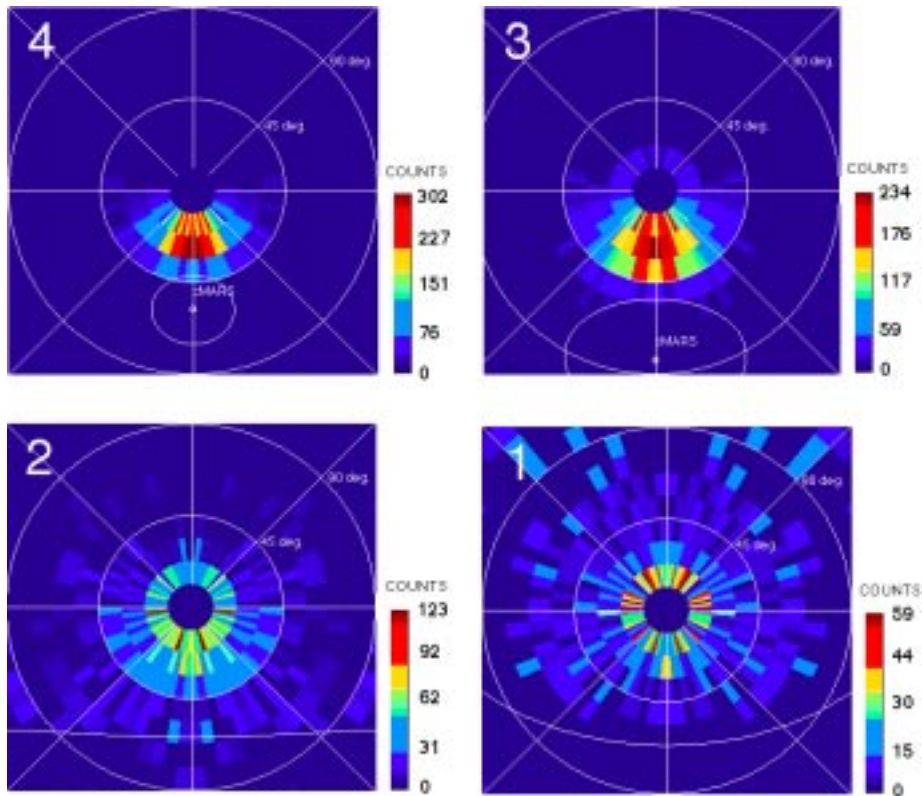


Figure 1.8.3. The simulated ENA images expected from NPI for four locations along the Mars Express orbit marked in the inset of Figure 1.3.1. The position 4 not shown in Figure 1.3.1 corresponds to the orbit apoapsis. The polar axis is looking towards the Sun. The solar wind ENAs are blocked.

The NPD sensor extends the ENA images in two new dimensions, mass and energy. Figure 1.8.4 shows the image of hydrogen atom fluxes expected from NPD at the point 2 of Figure 1.8.3 and two energy spectra corresponding to the marked pixels. The energy spectra supply direct information about the temperature and plasma bulk velocity in the interaction region and the magnetosphere.

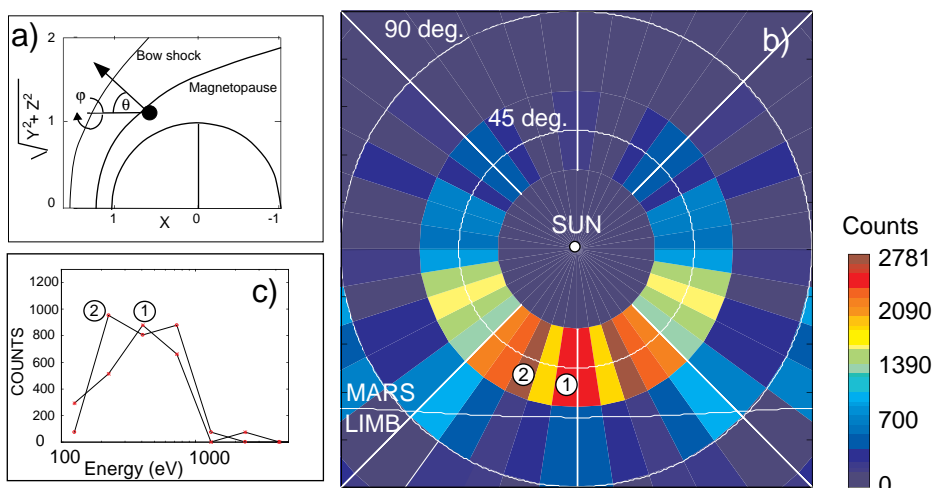


Figure 1.8.4. The simulated ENA image (b) and energy spectra from two marked pixels (c) expected from NPD. The inset (a) shows the spacecraft position and the coordinate system used. The integration time is 10 s.

By remotely measuring the energy of the accelerated planetary ions and global configuration of the escaping plasma, the NPD and NPI sensors allow a determination of the total ion outflow which the crucial parameter in understanding the atmospheric erosion process under the solar wind action. The new effects related to the solar wind - Mars interaction, ENA precipitation and ENA albedo, (Kallio *et al.*, 1997; Luhmann and Kozyra, 1991) have recently been predicted theoretically. The ASPERA-3 experiment will provide the first quantitative observations of these phenomena.

The polar elliptical orbit of the Mars Express does not allow *in situ* investigations of the plasma effects related to the possible Phobos outgassing and its hypothetical gas / dust torus (see review in Barabash, 1995c). The ASPERA-3 instrument with its remote capabilities will search for ENAs resulting from the charge - exchange of the Phobos gas environment with the shocked solar wind when the moon is inside the Martian bow shock.

The electron and ion measurements provide the input information on the solar wind for the models to be used for deconvolution of ENA images. In addition, EIS (ELS, IMA in the optional design) will provide new information regarding the nature of the Martian obstacle and other domains of the Martian magnetosphere because it is anticipated that the spacecraft will travel below the obstacle boundary (Figure 1.8.1).

ENA imaging from the $\sim 4 R_m$ apoapsis, away from the primary solar wind interaction region but close enough to keep the fluxes measurable, can allow a "global" view of Mars-space to be obtained while the ambient solar wind conditions are simultaneously sampled. Together, the ENA fluxes and solar wind conditions can be used to infer the energy deposition into the upper atmosphere. The consequences can be determined by modifying codes (e.g. Kozyra *et al.*, 1982; 1997) developed to study ring current particle energy deposition into Earth's upper atmosphere. The energy input from the oxygen pickup ions around Mars can also be inferred from these data (e.g. as in Luhmann and Kozyra, 1991) since the ENA flux gives information about the prevailing density of oxygen in the upper atmosphere (from which many ENAs originating at low-altitude are emitted, according to Kallio *et al.*, 1997). The energy deposition codes, adjusted for the Martian atmosphere, will yield altitude profiles that can be both compared with the photoelectron (i.e. solar) energy input profiles, and used as input to other codes to study any chemical or dynamical consequences.

1.9 Extracting Diagnostics Using ENA Images

In Sections 1.3 and 1.4, we have demonstrated, that ENA images will contain the signatures of the interaction of solar wind protons interacting with the Martian exosphere. Our scientific goal is to obtain information such as is illustrated in Figure 1.8.1. We will now outline how quantitative diagnostics of this complex interaction can be extracted from the ASPERA-3 ENA images. We base our approach on the success of a technique recently developed at JHU/APL by E. C. Roelof and A. J. Skinner for extracting energetic ion distributions from the ENA images to be obtained by the upcoming NASA magnetospheric imaging missions "IMAGE" (launch January 2000) and TWINS (launches in early 2002 and 2004).

The algorithm minimizes $\chi^2 = 1/N \sum (S_i - D_i)^2 / S_i$ where:

D_i = Data: counts measured in pixel i of the image ($i = 1, 2, \dots, N$)

S_i = Simulation: counts calculated in pixel i of the image ($i = 1, 2, \dots, N$)

The simulation is based on the instrument response function and line-of-sight integration of K -parameter analytic model $F(r, v; p_1, \dots, p_K)$ of ion uni-directional differential intensity (and exospheric neutral density). The algorithm utilizes scaled partial derivatives of the model (dp_k) $\partial F / \partial p_k$ to calculate components of "gradient" (dp_k) $\partial \ln \chi^2 / \partial p_k$ ($k=1, \dots, K$). When the model "converges" to the data, the statistical Poisson uncertainty $\langle D_i^2 \rangle \cong S_i$ so $\chi^2 \rightarrow 1$ and $\ln \chi^2 \rightarrow 0$. The algorithm combines three different *non-linear* minimization techniques in the context of estimated local topology of $\ln \chi^2$ in K -dimensional parameter space: Downhill simplex, Conjugate gradient, Hessian inversion. The appropriate technique is automatically selected for each step such that χ^2 decreases

monotonically *and* the local topology is favorable for the *next* step. The process is automatically re-initialized about any point of unfavorable topology.

Energetic ion distributions in the Earth's magnetosphere described by $K=32$ parameters are presently being extracted from simulated ENA images (1-minute exposure time) with $4^\circ \times 4^\circ$ angular resolution and instrument sensitivities corresponding to those ENA imagers being constructed for IMAGE and TWINS. The algorithm converges to the optimum parameter set after several hundred steps. Each step involves the simulation of one image (~2000 pixels), which, on a UNIX system workstation, takes 10 seconds per image. We anticipate a factor of 10 improvement in computation speed by the time of launch of these missions, so we expect that these parametrized ion distributions could be extracted as an automated standard data product every ~5 minutes.

For ENA images at Mars, the approach would be to utilize the multi-parameter empirical model of *Kallio* (1996) for the solar wind flow (Figure 1.8.1) and the model exosphere of *Krasnopolsky and Gladstone* (1996) (Figure 1.1.2) so that they could be incorporated into the minimization algorithm. The calculation of ENA intensities in the latter paper, and in this proposal, were carried out by Monte Carlo runs. They could also have been computed directly from analytic functions, each of which is characterized by a set of parameters. For example, the solar wind flow parameters are listed in Table 1 of *Kallio* (1996). With the angular resolution of NPI, it is only necessary to carry out, at most, a few line-of-sight integrals for each pixel:

$$j_{\text{ENA}}(r, \mathbf{v}) = \int ds \Sigma \sigma^{1,0}_{\mathbf{k}}(E) n_{\mathbf{k}}(r - \mathbf{u}s) F_{\text{SW}}(r - \mathbf{u}s, \mathbf{v}) \exp[-\int ds' \Sigma \sigma^{0,1}_{\mathbf{k}}(E) n_{\mathbf{k}}(r - \mathbf{u}s')] \quad (1)$$

where $\mathbf{u} = -\mathbf{v}/v$ and \mathbf{v} is the ENA (and, approximately, the solar wind proton) velocity. Here, $\sigma^{1,0}_{\mathbf{k}}(E)$ is the energy-dependent charge-exchange cross-section, and $\sigma^{0,1}_{\mathbf{k}}(E)$ is the corresponding stripping cross-section. *Roelof* (1997) has developed analytic approximations for the stripping integral in the exponential attenuation function, so only the main integral has to be carried out numerically. In the approximation used by *Kallio et al.* (1997), the solar wind flux can be written as a convected thermal phase space density characterized by a local density $N(r)$, temperature $T(r)$ and velocity vector $\mathbf{U}(r)$.

$$F_{\text{SW}}(r, \mathbf{v}) = N(r) [m/2\pi kT(r)]^{3/2} \exp\{-[m/2kT(r)] [\mathbf{v} - \mathbf{U}(r)]^2\}$$

The temperature is itself calculated from the local velocity and the properties of the upstream solar wind using a gas-dynamic law. If the streamline function is known, the local density may be calculated from the conservation equation by integrating along the streamline:

$$N(r) = N_0 \exp[-\int ds \nabla \cdot \mathbf{U}/U] \exp[-\int ds \Sigma n_i \sigma_i(E')]$$

where the integrals are carried out from $-\infty$ (well upstream where $N=N_0$) to the position r , or, equivalently and more practically, from r to $-\infty$. The energy $E' = mU^2/2$ varies along the streamline, but the cross-sections for H and O are nearly independent of energy, so the analytic approximations of *Roelof* (1997) can be used for the separable attenuation integral, as in (1). An additional approximation must be made for H₂, whose cross-section does depend weakly on energy.

As mentioned above, *Kallio* (1996) has parametrized the streamline function, so that all quantities are implicit functions of the solar wind input parameters. If the solar wind functions $N(r)$ and $\mathbf{U}(r)$ were available as explicit functions of the parameters, it would be computationally feasible to pick a set of input parameters for the solar wind stream function and the height dependence of the neutral ion exospheric densities, and then evaluate the line-of-sight integral in (1) within a reasonable amount of computing time. It is not unreasonable to expect that we can develop explicit parametric functions for the flow velocity $\mathbf{U}(r)$, and then in turn do the same for the derived function $\int ds \nabla \cdot \mathbf{U}/U$. This would directly give us $N(r)$ as an explicit function of the interaction parameters. Because the Monte Carlo calculations (Figure 1.3.1) indicate that the energy spectrum is relatively flat below the energy corresponding to the incident solar wind, the line-of-sight integrals for the NPI pixels need

not be evaluated for more than a few different energies. Consequently, only a few “typical” energies would also suffice for the NPD, as can be seen from Figure 1.8.3. This calculation, done for every pixel to be analyzed (but obviously not for pixels with insignificant counts), would constitute the simulated image, and would be the input to the minimization algorithm. An important check of the validity of the parameter set would be the consistency of the parameters extracted from a sequence of images from different positions along the same orbit, as illustrated in Figure 1.3.2,

We have laid out a program by which we could characterize the interaction of the solar wind flow with the Martian exosphere by a set of parameters, and then extract those parameters from the ENA images. Our present experience, derived from the techniques that have been developed to extract magnetospheric energetic ion distributions from the ENA images to be obtained from the upcoming NASA IMAGE and TWINS missions, points the way to extracting quantitative diagnostics from the ASPERA-3 ENA images.

2. Proposed Investigation in Context of Other Missions

The ASPERA-3 instrument will perform the first ENA imaging of another planet in the low energy range. No instruments with similar scientific objectives and capabilities have been or are planned to be flown to the other planets. The only similar experiment, ASPERA-C, was on-board the failed Mars - 96 mission. However the ASPERA-C did not have the ENA energy analyzing detector NPD. The Japanese PLANET - B mission to be launched to Mars during 1998 is concentrating on plasma measurements at Mars and does not include in its payload any ENA instrumentation.

As far as the Earth environment is concerned, the PIPPI instrument for the Astrid microsatellite comprised only the NPI sensor and was not able to measure the ENA energy in the low energy range. The LENA (Low Energy Neutral Atom) imager on-board the NASA IMAGE missions (Imager for Magnetopause - to - Aurora Global Exploration) covers a somewhat similar energy range 10 - 300 eV with 80% energy resolution and has a slightly better angular resolution of $8^\circ \times 8^\circ$ (Burch, 1995) than ASPERA-3. However, the total mass of the LENA instrument (22 kg) does not allow one to consider similar instrumentation for interplanetary missions.

In light of the above, we conclude that it is very important for the Mars Express mission to contain an ENA instrument which can investigate the coupling between the interplanetary medium and planetary neutral environment by a completely new method.

3. Technical Description

3.1 Overview

The ASPERA-3 experiment is designed for the analysis of ENAs, electrons, and ions with a complete coverage of the unit sphere. Mechanically, in the baseline configuration, the ASPERA-3 consists of a single unit which comprises three sensors, NPI, NPD, EIS, and a digital processing unit located on the scanner. All mechanical and electrical interfaces are made through the scanner. Figure 3.1.1. shows the basic instrument configuration and Figure 3.1.2 illustrates the ASPERA-3 sensor fields of view and the scan direction. Table 3.1.1 summarizes the experiment mechanical characteristics.

Table 3.1.1. The ASPERA-3 overview characteristics

Parameter	Baseline	Optional design
Mass, kg	5.95	7.85
Dimensions, mm (including rotation)	$379 \times 433 \times 234$	$359 \times 393 \times 234$ (main unit) $255 \times 150 \times 150$ (IMA)
Power	6.4	9.3

In the optional configuration, the ASPERA-3 experiment contains one extra sensor the Ion Mass Analyzer (IMA) which is a separate mechanical unit. Figure 3.1.2 also illustrates the IMA field of view. The electron and ion spectrometer EIS is reduced to the electron spectrometer ELS.

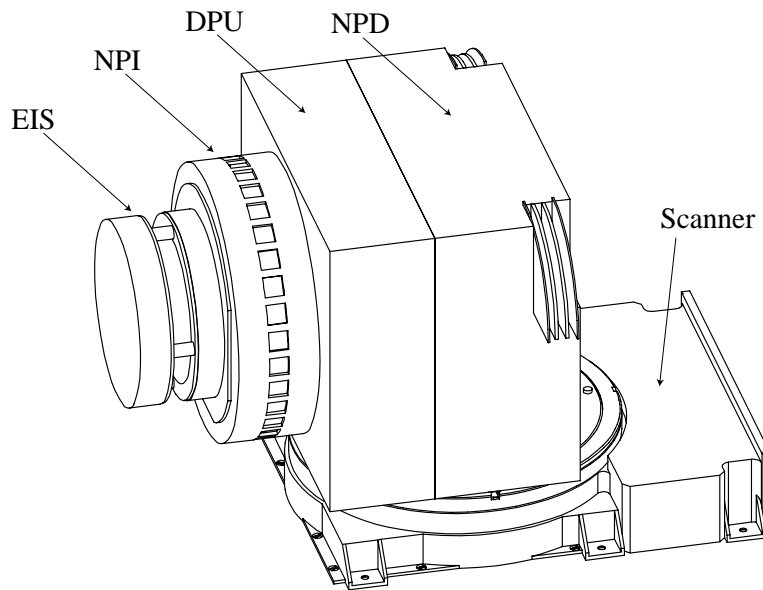


Figure 3.1.1. The ASPERA-3 basic configuration.

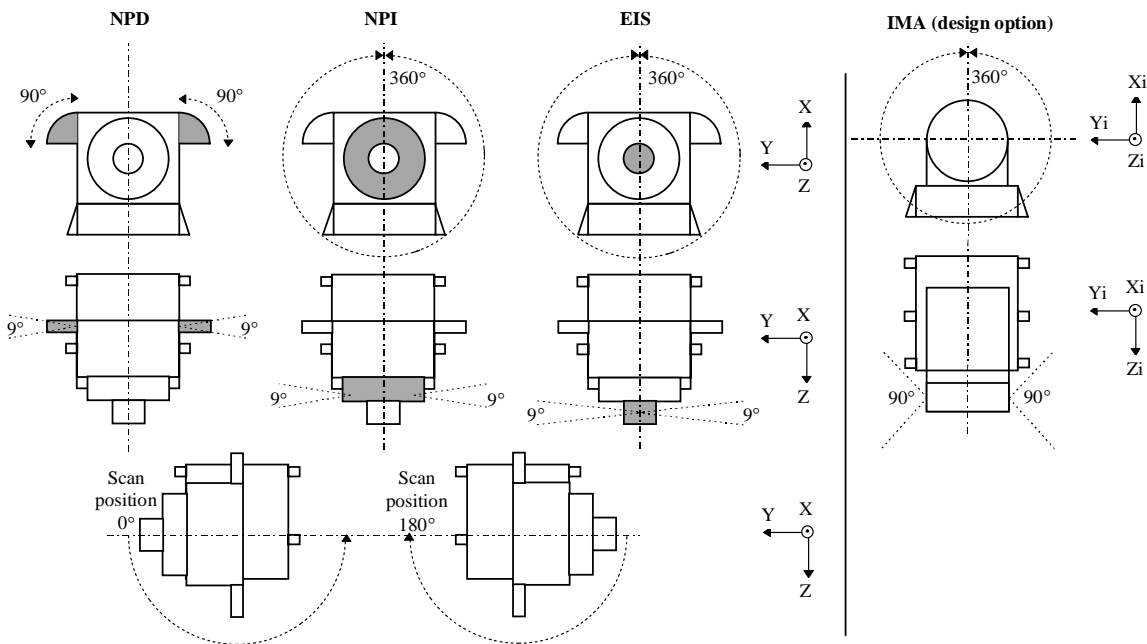


Figure 3.1.2. The ASPERA-3 sensors fields of view, the scan direction, and the instrument coordinate system. The IMA sensor (optional design) field of view is also shown.

3.2 Neutral Particle Imager. NPI

The NPI head is a replica of the NPI - MCP sensor developed for the ASPERA - C experiment on the Mars - 96 mission and successfully flown on the Swedish microsatellite Astrid launched in 1995 (*Barabash et al., 1998*). Figure 3.2.1 shows the images obtained by PIPPI - MCP and revealing

intense fluxes of ENAs (up to $10^6 \text{ cm}^{-2}\text{sr}^{-1}\text{s}^{-1}$) with energy less than 15 keV (Barabash et al., 1996) coming out from the exobase.

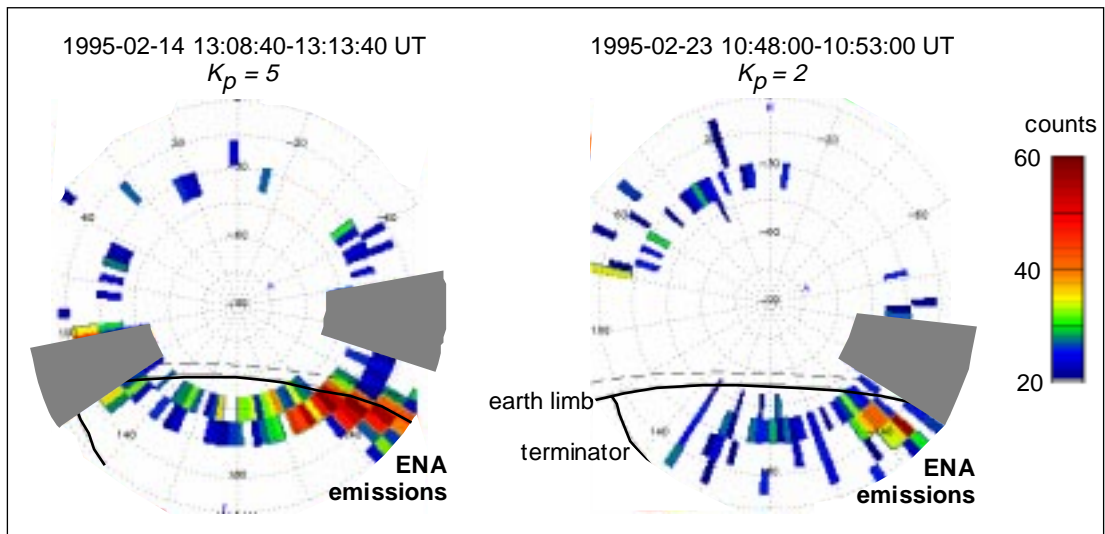


Figure 3.2.1. ENA images obtained by the PIPPI - MCP / Astrid sensor identical to NPI proposed for the Mars Express mission. The Astrid spacecraft was near the Pole at an altitude of 1000 km. The low energy ($< 15 \text{ keV}$) ENA emissions come from the exobase at the dusk sector. The images are for two different magnetospheric conditions, as indicated by K_p .



Figure 3.2.2. The low energy neutral particle imager for the ASPERA-C/Mars-96 experiment (spare unit).

In the NPI the charged particles, electrons and ions, are removed by the electrostatic deflection system which consists of two disks separated by a 3 mm gap (Figures 3.2.2 and 3.2.3). The 5 kV potential between the grounded and biased disks results in a strong electric field which sweeps away all charged particles with energies up to 60 keV. Since the integral ENA flux substantially exceeds the charged particle flux for energies greater than 60 keV, this rejection energy is

sufficient for satisfactory performance. The disks also collimate the incoming beam in the elevation angle. The space between the disks is divided into 32 sectors by plastic spokes forming 32 azimuthal collimators with an aperture of $9^\circ \times 18^\circ$ each. Neutrals passing through the deflection system hit a 32 sided cone target with a grazing (20°) angle of incidence. The interaction with the target results in the secondary particle production, both electrons and ions, and / or reflection of the primary neutrals. The particles leaving the target block are detected by a MCP stack in the Z configuration with 32 anodes. The signal from the MCP gives the direction of the primary incoming neutral. The MCP operates in ion mode with negative bias and thus detects (a) sputtered ions of the target material, (b) ions resulting from stripping of the primary neutrals, and (c) neutrals reflected from the target surface. In order to improve the angular resolution and collimate the particles leaving the interaction surface, 32 separating walls are attached to the target forming a star-like structure. This configuration allows the entering particles to experience multiple reflections and reach the MCP. NPI covers 4π in

one instrument scan and produces an image of the LENA distribution in the form of an azimuth \times elevation matrix. The direction vector of 32 elements is read out once every 62.5 ms.

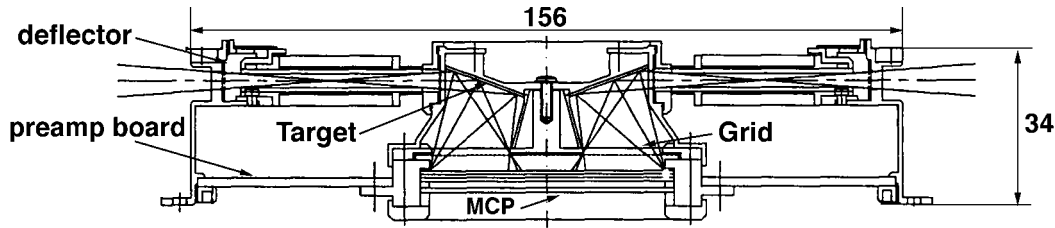


Figure 3.2.3. *The NPI sensor cross section.*

An important issue in the NPI design is the selection of a coating for the target which will suppress ever present flux of UV photons which enter the instrument and produce the UV background. NPI uses the same coating as in the PIPPI and ASPERA-C experiments, namely, DAG 213, a resin - based graphite dispersion. This is similar to Aquadag which is a graphite dispersion in water. This coating demonstrated satisfactory performance in the PIPPI experiment flown in the Earth's magnetosphere. The averaged background resulting from Lyman - α radiation of the terrestrial hydrogen corona and energetic charged particles was found to be 3 cnts/s pixel and the MCP dark noise less than 0.05 cnts/s pixel. Scaling down the solar flux by a factor of 3 and the linear sizes by a factor of $6400 / 3400 = 1.9$ we will expect the UV intensity to cause the MCP background to be at least 5 times less for the Martian conditions than for the Earth. The background count rate is expected to be 0.6 counts/s/sector. Using the 0.6% efficiency defined in the PIPPI-MCP calibrations we arrive at a sensitivity of $4 \times 10^4 \text{ cm}^{-2}\text{sr}^{-1}\text{s}^{-1}$ which is sufficient to image the solar wind interaction region on Mars where one expects ENA fluxes well above $10^5 \text{ cm}^{-2}\text{sr}^{-1}\text{s}^{-1}$ (section 1.7).

NPI uses the 56 mm MCP plates utilized in the PIPPI / ASTRID, ASPERA-C / Mars-96 experiments. We plan to use the same MOCAD preamplifiers as in the ICA experiment for the ESA Rosetta mission. A summary of the instrument characteristics is given in Table 3.2.1.

Table 3.2.1. The NPI Sensor Characteristics

Parameter	Value
Energy range	$\sim 0.1 - 60 \text{ keV}$
Energy resolution	No
Angular resolution (FWHM)	$4.6^\circ \times 11.5^\circ$
Aperture per sensor	$9^\circ \times 18^\circ$
Full field of view	$9^\circ \times 344^\circ$
Azimuthal sectors	32
Geometrical factor	$7.8 \times 10^{-2} \text{ cm}^2\text{sr}$
Geometrical factor per sector	$2.5 \times 10^{-3} \text{ cm}^2\text{sr}$
Efficiency	$\approx 1 \%$
Power	0.8 W
Mass	0.7 kg

3.3 Neutral Particle Detector. NPD

The ASPERA-3 experiment utilizes a combination of two sensors to perform comprehensive measurements of ENAs. The NPI sensor surveys ENA fluxes with sufficiently high angular resolution while the NPD sensor performs the velocity and mass measurements.

In modern ENA instrumentation there are two techniques which may be applicable for energy / mass resolving measurements of neutrals in the energy range 100 eV - 10 keV. These are ENA ionization using an ultra - thin carbon foil and ionization using surface conversion (see review by *Gruntman*, 1997). Neither of these techniques can be employed in an experiment for the Mars Express mission due to severe mass and volume constraints and the absence of the space - flight proven components. However, very high ENA fluxes at Mars and lower UV background allow us the use of another approach based on the quasi- specular reflection from surfaces under grazing angles of incident (a somewhat similar technique was considered by *Herrero and Smith*, 1992). The surfaces to be used (graphite and stainless steel) are easily available, do not require any in-flight maintenance procedures, and guarantee reliable performance over the mission duration. The chosen technique is not based on any advanced technologies which would require significant development work.

The NPD sensor consists of two identical detectors each of which is a pin-hole camera. Figure 3.3.1 provides a three-dimensional view of the two detectors along with an ENA trajectory.

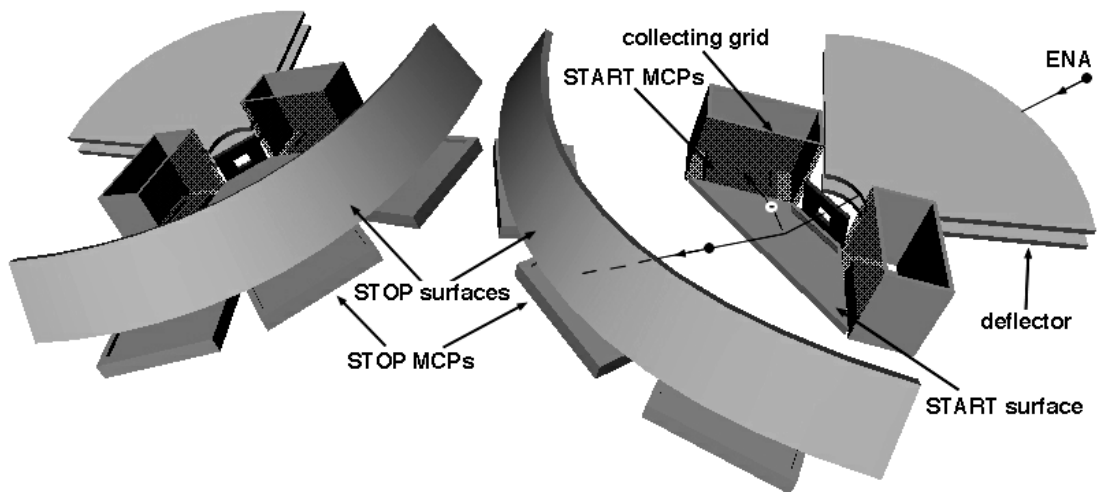


Figure 3.3.1. *Three-dimensional view of the NPD principal components.*

In each detector the charged particles, electrons and ions, are removed by the deflection system which consists of two 90° sectors separated by a 4.5 mm gap. The deflection system is also equipped with broom magnets (not shown) to remove electrons. This makes it possible to operate the NPD in an ion detection mode for in-flight calibrations. In the normal operational mode the 8 kV potential applied to the disks and the resulting strong electric field sweeps away all charged particles with energies up to 70 keV. The deflector also collimates the incoming beam in the elevation angle. The collimated ENA beam emerging from the $4.5 \times 4.5 \text{ mm}^2$ pin - hole hits the START surface under the grazing angle 20° and causes the secondary electron emission. By a system of collecting grids, the secondary electrons (SE) are transported to one of two MCP assemblies giving the START signal for the time-of-flight (TOF) electronics. The configuration of the START surface, START MCPs, and the collecting grids is shown in Figure 3.3.2 which also demonstrates the traced secondary electron trajectories. In this configuration, the MCP stack is located 7 mm above the START surface to minimize the flux of reflected photons which could reach the plates and increase the electron optic transmittance.

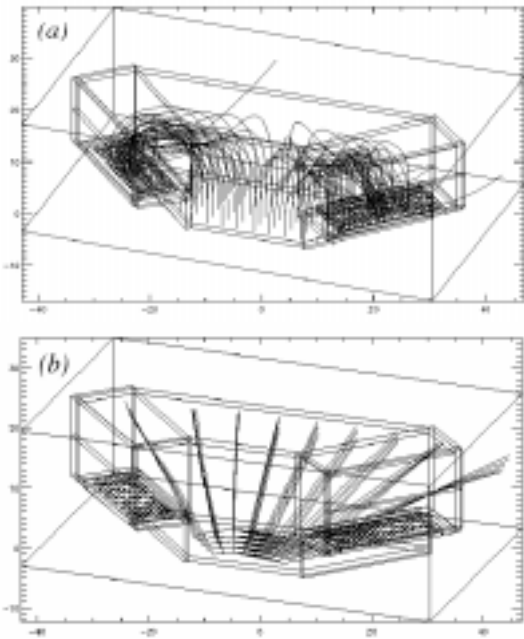


Figure 3.3.2. The START surface with collecting grids and trajectories traced for (a) secondary electrons and (b) reflected 80 eV ions.

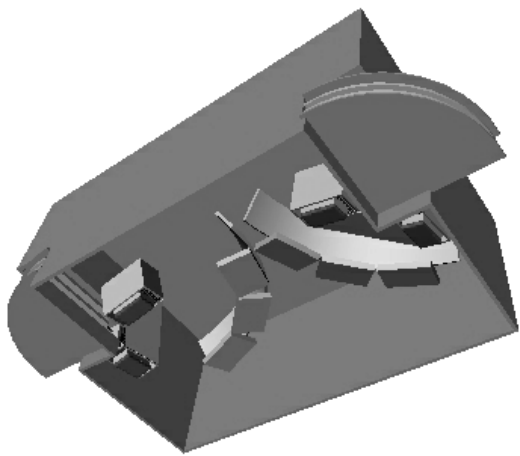


Figure 3.3.3. Cut-away view of the NPD sensor.

stability under long - time particle exposure (Barabash, 1995c). The STOP surface material is not very crucial because the SE yield does not depend strongly on the target Z. However, heavier targets are slightly superior (Benzeth, 1982) and the STOP surface is made of stainless steel. Table 3.3.1 gives the "design-goal" surface characteristics for the hydrogen ENAs over the energy range 100 eV - 10 keV. The numbers will be defined more exactly during development phase. Note, that grazing incidence on the START surface results in higher SE yields than normal incidence.

The electric field created by the distributed potentials of collecting (+50V, +20V), repelling (-12V), and grounded grids as well as the MCP front side (+200 V) provides the efficient (98%) collection of the secondary electrons onto the plates. The incident ENAs are reflected from the START surface near-specularly. Since the charge state equilibrium is established during the interaction with the surface, the emerging beam contains both the neutral and ionized (positive and negative) components. To increase the total efficiency, no further separation by the charge is made. As proven by the ion tracing, there is very little disturbance to the reflected atomic ions leaving the START surface with an energy above 80 eV, introduced by the START electron optics. Therefore particles of all charge states - negative, neutral, and positive - will impact the second surface, the STOP surface, and again produce secondary electrons which are detected by one of the three MCP assemblies giving the STOP signal. The time of flight over the fixed distance of 8 cm defines the particle velocity. The STOP MCPs also give the azimuthal direction. Since the SE yield depends on mass for the same velocity, the pulse height distribution analysis of the START signals (the MCP charge) provides the estimation of ENA mass. Each event is stored in the array START MCP charge \times time-of-flight \times direction. The array is accumulated over the sampling time 62.5 ms. Figure 3.3.3 shows a cut-away view of the NPD sensor.

The UV suppression in NPD is based on the START surface coating and the coincidence of START / STOP signals. Based upon our experience in the development of the ASPERA - C / Mars-96 and PIPPI-MCP / Astrid experiments we decided to use DAG 213, a resin - base graphite dispersion (which is similar to Aquadag,) for the START surface coating. The plate itself is made of aluminum. This combination has a low light reflection coefficient and low photoelectron yield but yet a sufficient secondary electron yield (see Table 3.3.1). This coating has also demonstrated good

Table 3.3.1. The START / STOP surface characteristics

Parameter	Value	Comment / Reference
SE yield for the START surface, γ_{ENA}^{START}	0.05 - 3	Estimated on the basis of data for metals (<i>Chamres</i> , 1964; <i>Coggiola</i> , 1986)
Particle reflection coefficient for the START surface, ρ^{START}	0.7 - 0.5	Estimated
Photoelectron yield (Lyman α) for the START surface, γ_{UV}^{START}	0.01	DAG 213 shows similar photoelectric properties as Aquadag (T. Harley, IRF Uppsala, private communication) For Aquadag see <i>Grard</i> , (1973)
UV reflection coefficient for the START surface, α^{START}	0.06	Carbon black-acrylic resin (<i>ESA (TST-02)</i> , 1979)
SE yield for the STOP surface, γ_{ENA}^{STOP}	0.2 - 2.5	<i>Benazeth</i> , 1982
Photoelectron yield (Lyman α) for the STOP surface γ_{UV}^{STOP}	0.01	<i>Grard</i> , (1973)
UV reflection coefficient for the surrounding, α^{box}	0.02	Black copper (A. Fedorov, IKI, Moscow, private communication)
MCP efficiency for UV photons, ϵ_{UV}	0.01	
MCP efficiency for 200 eV electrons ϵ_{EL}	1.0	Phillips component book, 1991
Collecting grid transmittance, ϵ_{GR}	0.95	

For the given geometrical factor, G , and the energy window, ΔE , the ENA differential flux j_{ENA} results in the count rate N_{ENA} ,

$$N_{ENA} = G j_{ENA} \Delta E \gamma_{SEE}^{START, STOP} \rho^{START} \epsilon_{GR}$$

The 100% MCP efficiency for the electrons was not included. The UV photons produce the count rates $N_{UV, START}$ and $N_{UV, STOP}$ in the START and STOP channels, respectively. The counts in the START channel result from the photoelectrons, double reflected photons (the surface - the surrounding), and photoelectrons from the double reflected photons

$$N_{UV, START} = G J_{UV} (\epsilon_{GR} \gamma_{UV}^{START} + \alpha^{START} \alpha^{box} \epsilon_{UV} + \alpha^{START} \alpha^{box} \gamma_{UV}^{START}) \approx G J_{UV} \epsilon_{GR} \gamma_{UV}^{START}.$$

Here we assume the corresponding view factors to be unity. The counts in the STOP channel are produced by (a) the photoelectrons from the photons reflected from the START surface and (b) the doubly-reflected photons directly impacting the MCP.

$$N_{UV, STOP} = G J_{UV} (F_{SS} \alpha^{START, STOP} \gamma_{UV}^{STOP} + \alpha^{START} \alpha^{box} \epsilon_{UV}) \approx G J_{UV} F_{SS} \alpha^{START} \gamma_{UV}^{STOP}$$

$F_{SS} = 0.011$ is the view factor between the START and STOP surfaces. The resulting accidental coincidence count rate caused by photons, N_{UV} , is

$$N_{UV} = N_{UV, START} N_{UV, STOP} \tau$$

where $\tau = 1.56 \mu\text{s}$ is the time the STOP channel is open for triggering. This time is defined by the slowest (300 eV) oxygen atoms travelling the time-of-flight distance. Figure 3.3.4 presents the expected count rates calculated for the values from Table 3.3.1 for different ENA and UV fluxes. The Lyman α observations made on Mariner 6, 7, 9 (Anderson, 1974) and Mars 2, 3 (Dementyeva et al., 1972) revealed the maximum Lyman α emission intensity to be 4 kR which would result in a UV background of 0.3 cnts/s. The direction with the brightest Lyman α emissions corresponds to the line-of-sight along the planetary limb. The lowest ENA flux above the UV background is about $10^5 \text{ cm}^{-2}\text{s}^{-1}\text{sr}^{-1}\text{keV}^{-1}$ for 100 eV. This applies for the particular configurations when the Mars limb within the NPD field of view. For all other directions it is $10^4 \text{ cm}^{-2}\text{s}^{-1}\text{sr}^{-1}\text{keV}^{-1}$ and, therefore, sufficient to meet the requirements listed in Table 1.5.1.

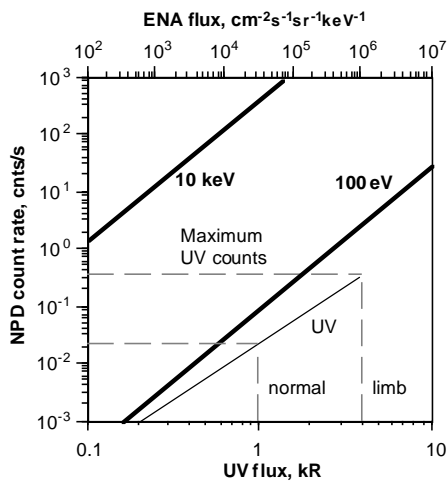


Figure 3.3.4. The UV background and ENA count rates expected for the NPD minimum and maximum energies

The velocity resolution of the instrument is defined by three factors: geometrical path length variations in the TOF system ($\Delta L/L$), energy straggling during particle - START surface interaction ($\Delta E/E$), and timing errors ($\Delta T/T$). In order to estimate the first factor we have performed simulations of the NPD sensor geometry. The STOP surface shape was assumed to be spherical with a 8 cm radius around the START surface center and the 14° central angle. Figure 3.3.5 shows the matrix of the maximum $\Delta L/L$ values for each azimuth and elevation of incidence within the instrument's field of view for the specularly reflected particles. The average value is about 8% for the geometry in question.

The timing error ΔT defined by the TOF electronics and the time of flight dispersion of the START / STOP electrons does not exceed 1 ns. Thus, the relative timing error $\Delta T/T$ is less than 2%.

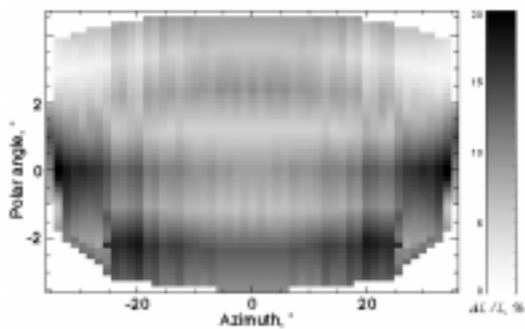


Figure 3.3.5. The matrix of maximum path length variations for each azimuth and polar angle within the instrument's field of view.

The spread in energy of the reflected ions does not exceed twice the energy loss due to the interaction process. The latter can be estimated to be less than 60% for energies less than 1 keV (Herrero and Smith, 1992) but increases with the ENA energy due to deeper penetration into the surface material. The exact value which will be defined by calibration is expected to be less than 80%. The total velocity resolution given as the square root of the sum of the squared errors is about 40%, i.e., the energy resolution is 80% for a fixed mass.

The requirements for mass resolution are rather modest as compared to a typical plasma instrument. It is sufficient to resolve H and O only. The planetary helium ion densities are much lower than those for oxygen (Barabash et al, 1995a) and the corresponding flux of the helium ENAs is low. Since the SE emission has a threshold of about $6 \times 10^6 \text{ cm/s}$, the oxygen atoms can only be detected from about 300 eV. For the higher particle velocities, the differences in the SE yield from the START surface for H and O reaches a factor of 2 for the same velocity. Thus, an MCP assembly with a high pulse - height resolution (30%) operating in non-saturated mode is able to perform the hydrogen -oxygen mass identification.

The NPD sensor electronic block diagram is shown in Figure 3.3.6. The TOF electronics are based upon a novel, innovative design. They incorporate a flip-flop chain, with each cell having a fixed time-delay. The start signal from the Start-MCP will trigger the chain which will count up to

the stop pulse. The final count (TOF) is evaluated by digitally reading the flip-flop outputs. In order to minimize timing tolerance, the integrated LSI device will be fully temperature controlled. The system has already been developed and tested under contract from the MP Ae at the University of

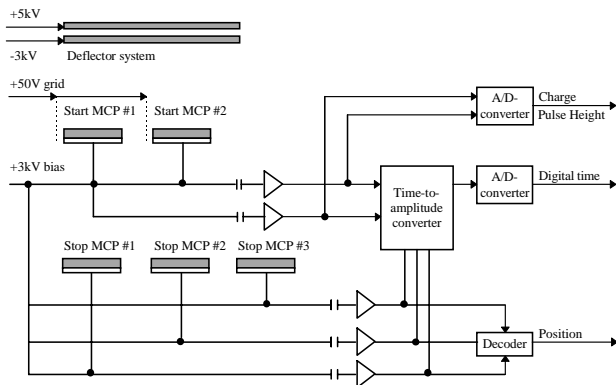


Figure 3.3.6. The NPD electronics block diagram

direction information (3 bits), the pulse-height analyzed signal providing mass resolution (10 bits), and the TOF giving the energy spectral information (10 bits). This output will be further processed by the DPU.

Table 3.3.2 sums up the NPD characteristics.

Table 3.3.2. The NPD Sensor Characteristics

Parameter	Value
Energy range	100 eV- 10 keV (H) 300 eV - < 100 keV (O)
Energy resolution (H)	0.8 (16 steps)
Mass resolution	H, O (8 steps)
Aperture per pixel	9° × 30°
Full field of view	9° × 180°
Azimuthal sectors	2 × 3
Geometrical factor	3.4 × 10 ⁻² cm ² sr
Geometrical factor per pixel	6.2 × 10 ⁻³ cm ² sr (central) 5.3 × 10 ⁻³ cm ² sr (side)
Efficiency (H, 100 eV - 10 keV)	1 - 50%
Power	1.5 W
Mass	1.8 kg

3.4 Electron and Ion Spectrometer. EIS

The Electron and Ion Spectrometer (EIS) sensor represents a new generation of ultra-light, low-power, combined ion-electron sensors. It is formed by two spherical electrostatic analyzers sharing a common symmetric top-hat and collimator system (Figures 3.4.1, 3.4.2). Particles enter the common aperture at any angle in the plane of incidence. Electrons and ions are then deflected into their respective spectrometer by applying a positive voltage to the inner electron plate and a negative voltage to the inner ion spherical deflection plate. The particles hit a micro-channel plate (MCP) after being filtered in energy by the analyzer plates. The plates are stepped in voltage to achieve an energy spectrum. The hits are detected by anodes and preamplifiers connected to registers and the number of hits per sample interval are then further processed in the data processing unit (DPU).

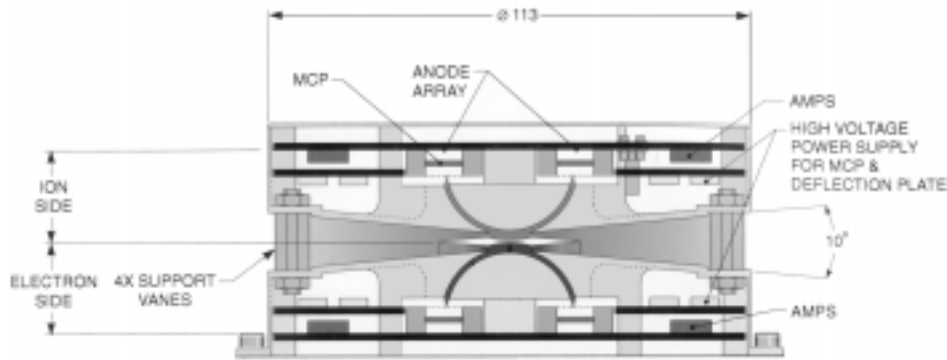


Figure 3.4.1. *The EIS sensor unit.*

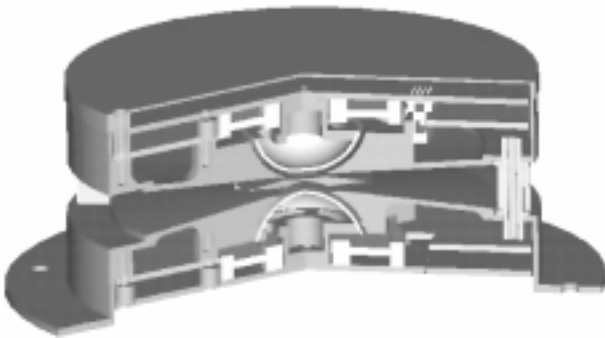


Figure 3.4.2. *Cut-away view of EIS.*

Electrons and ions with energies up to 20 keV/q will be measured simultaneously, with a maximum time resolution of 16 energy sweeps per second for electrons, and 8 sweeps per second for ions. Each top-hat analyzer uniquely resolves the angle of arrival in the plane of the top-hat uniquely by focusing the particles at the exit to the analyzer. There are 16 anodes, each defining a 22.5° sector, behind the electron and ion MCPs each of which is connected to a preamplifier. The EIS sensor will be mounted

on the ASPERA-3 scan platform in such a way that the full 4π angular distribution of electrons and ions will be measured during each platform scan.

The first version of this instrument, MEDUSA, will be flown on the Swedish Astrid-2 and Munin micro-satellites during 1998.

Table 3.4.1. The EIS characteristics

Parameter	Value
Mass	0.60 kg
Power	1.2 W
Dimensions	113 mm (diameter) \times 54 mm (height)
Raw telemetry bit rate	16 kbps
Energy range (electrons and ions)	10 eV/q – 20 keV/q
Energy resolution ($\Delta E/E$)	25% (e), 8% (ions)
Energy steps per sweep	32 (e), 96 (ions)
Acceptance angles	$360^\circ \times 10^\circ$
Geometric factor	$3 \times 10^{-4} \text{ cm}^2 \text{ sr}$ (el), $1 \times 10^{-4} \text{ cm}^2 \text{ sr}$ (ions)

3.5 Ion Mass Analyzer. IMA (design option)

To provide mass resolution of ions, this proposal includes the following option:

- A mass resolving spectrograph, the Ion Mass Analyzer (IMA) is included in ASPERA-3.
- The ion part of the Electron and Ion Spectrometer (EIS) is removed from ASPERA-3.

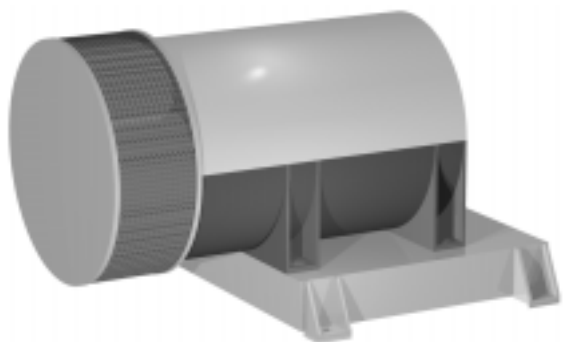


Figure 3.5.1. *The Ion Mass Analyzer (IMA).*

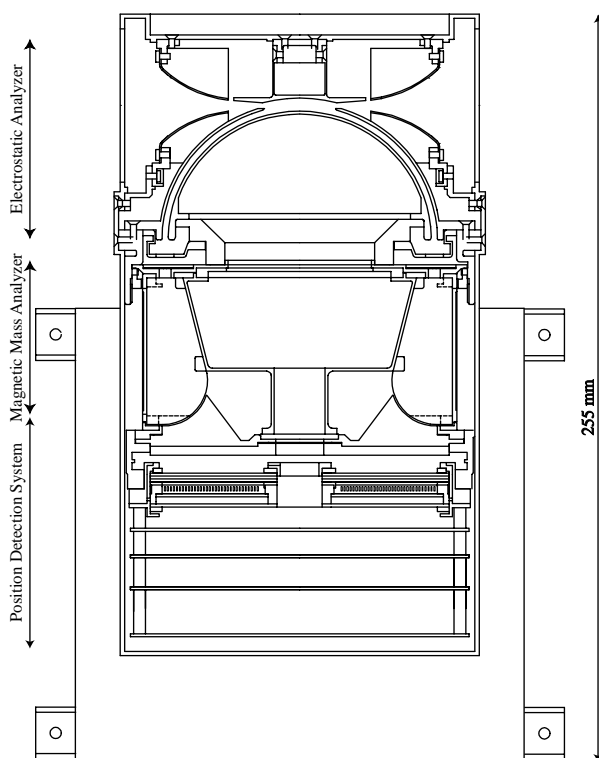


Figure 3.5.2. *Cross section of IMA.*

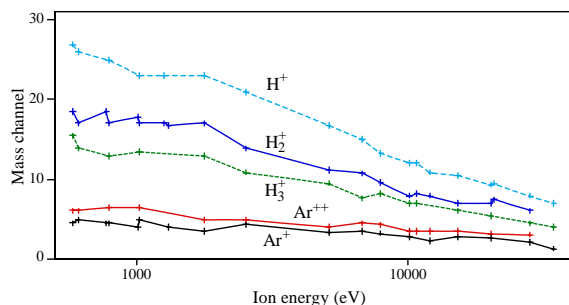


Figure 3.5.3. *Calibration results for the IMI instrument on board the Planet-B spacecraft.*

The Ion Mass Analyzer (Figure 3.5.1. and 3.5.2.) is an improved version of the ion mass spectrographs TICS (Freja, 1992), IMIS (part of ASPERA-C, Mars-96, 1996), and IMI (Planet-B, 1998). It is an exact copy of the ICA instrument to be flown on Rosetta to comet Wirtanen in 2003. Particles enter the analyzer through an outer grounded grid. Behind the grid is a deflection system whose purpose is to deflect particles coming from angles lying between 45° and 135° with respect to the instrument symmetry axis, into the electrostatic analyzer (ESA). Ions within a swept energy pass band will pass the ESA. The ions are then deflected in a cylindrical magnetic field set up by permanent magnets. The field deflects lighter ions more than heavy ions into the center of the analyzer. The ions finally hit a micro-channel plate (MCP) and are detected by an anode system. Ions are simultaneously analyzed regarding both direction and mass per charge. The magnet assembly can be biased with respect to the ESA to post-accelerate ions. This post-acceleration enables a selection of both mass range and mass resolution.

The electrons from the MCP are detected by an "imaging" anode system. A system of 32 concentric rings behind the MCP measures the radial impact position (representing ion mass), whereas 16 sector anodes measure the azimuthal impact position (representing ion entrance angle). In our recent instrument on board Planet-B we used an analog detection system for impact location. For Rosetta and Mars Express we will employ a digital system which gives improved mass- and angular-resolution. Even with the analogue system, we have good mass resolution as shown in Figure 3.5.3. The mass detection technique utilized by IMA is ideal for the detection of ions of all masses (1 to $\approx 10^6$ a.m.u.), including sub-micron sized "dusty" plasma components, a relatively unexplored plasma component believed to be of great importance in some cosmogonic scenarios. The characteristics of the IMA instrument proposed as an optional mass spectrograph for Mars Express are summarized in Table 3.5.1.

IMA will be an exact copy of the ICA instrument developed for Rosetta. The time schedule for the Mars Express mission would allow the fabrication, testing, and calibration of

Table 3.5.1. IMA Characteristics

Parameter	Value
Mass	2.2 kg
Power	3.5 W
Dimensions	255 x 150 x 150 (l x w x h)
Energy range	1 eV/q - 40 keV/q (in 128 steps)
Energy resolution	$\Delta E/E = 0.07$
Total field-of-view	360° x 90°
Angular resolution	22.5° x 4.5°
G - factor / sector	3.5×10^{-4} (cm ² sr)

an additional unit in parallel with the fabrication of the two Rosetta flight models.

In summary, the following unique features of IMA will contribute to the understanding of the Martian plasma environment:

- High angular resolution and 360° field of view, combined with the 90° entrance deflection system provides coverage of a large part of the unit sphere.
- Sufficient mass resolution and low "ghost" background for cold plasma (<1 keV).
- High dynamic range for fluxes, count rate dynamic range >10⁶ counts per second.
- High sensitivity and good background immunity using the coincidence technique will eliminate the background to <10⁻¹ cnts/s.

3.6 Electron Spectrometer. ELS (design option)

In the optional configuration positive ions are measured with mass resolution by the Ion Mass Analyzer (IMA). There is thus no need to have a separate ion spectrometer without mass resolution, and therefore the EIS part of ASPERA-3 can be reduced to contain only the electron spectrometer.

**Figure 3.6.1.** Cut-away view of ELS.

Since EIS is completely modular, with only the top-hat shared by the electron and ion parts, the ion part can be removed from the instrument.

The electron measurements of ELS will be exactly the same as those made by EIS, the only parameters that will change are the mass, power and telemetry requirements. The characteristics valid for ELS are given in Table 3.6.1.

Table 3.6.1. The ELS instrument characteristics

Parameter	Value
Mass	0.30 kg
Power	0.6 W
Dimensions	113 mm (diameter) x 36 mm (height)
Raw telemetry bit rate	8 kbps
Energy range	10 eV/q – 20 keV/q (in 32 steps)
Energy resolution, $\Delta E/E$	25%
Acceptance angles	360° x 10°
Geometric factor	3×10^{-4} cm ² sr

3.7 Scanner

The scanning platform (scanner) to be used in the ASPERA-3 experiment was developed for the ASPERA-C instrument for the Mars-96 mission.

The scanner interfaces the sensor head unit with the satellite mechanical and electrical subsystems and includes the following elements:

- worm screw between two redundant stepper motors driving a large diameter worm wheel
- four electronic boards for motor control and sensor interface

- two position sensor to determine positions 0 and 180 degrees and one for determination of intermediate angles
- feed-through cable loop with six cables and 12 connectors, each cable with 26 conductors (a maximum of 312 connections possible) interfacing through 3 D-SUB or MDM connectors to the satellite electronic subsystem
- large diameter angular contact ball bearing
- housing and circular sensor platform manufactured in high-strength aluminum alloy.

A worm gear type of mechanism was selected in order to provide self-locking without electrical power, to minimize friction and to obtain a high gear ratio. The platform is made as a plug-in unit towards the sensor head unit. Great efforts have been spent to reduce mass, volume, power consumption and outgassing in vacuum as well as to achieve high reliability. On command the platform can be turned to an arbitrary position or to scan continuously at any rate of rotation up to maximum. The pre-selected 0° - 180° scan periods are 32, 64, and 128 s.

Table 3.7.1 provides the scanner technical characteristics.

Table 3.7.1. The ASPERA-3 scanner data

Technical data	Value
Maximum angle of rotation, °	+/-90
Angular movement per step, full step mode, °	0.0190
Angular movement per step, half step. mode, °	0.0095
Angular position feedback resolution, °	0.05
Angular positioning accuracy, °	0.2
Operational rotation rate, °/s	1.5/3.0/6.0
Maximum rotation rate, °/s	25
Platform load, kg	6.3
Maximum platform load, kg	~12
Dimensions, mm	44×200× 273
Power, W	0.5 - 2.0
Mass, kg	1.85
Operational lifetime in vacuum	>3

3.8 Digital Processing Unit. DPU

The ASPERA-3 digital processing unit (DPU) for the Mars Express mission will be based on the ICA (Ion Composition Analyzer) DPU for the ESA Rosetta mission. The ASPERA-3 DPU will be built by the same team at FMI that designs and manufactures the ICA DPU. The DPU comprises the following components:

- TMS320C50 CPU running at 40MHz (TBC)
- 32kB RAM (4pcs 8k × 8 or 2pcs 16k × 8)
- 32kB PROM (4pcs 8k × 8)
- 32kB EEPROM (1pcs 32k × 8)
- 2MB mass memory (4pcs 512k × 8)
- ACTEL RH1020 (2-3pcs)
- Telemetry (TM) and telecommand (TC) drivers

The large memories (mass memories) are used as telemetry buffer (FIFO style). The ACTEL RH1020 are used for telemetry and command interfaces with the drivers and receivers on S/C interfacing lines and for internal address and data encoding and decoding. If the Texas TMS320C50 will not be qualified (qualification program running under the ICA/LAP development for the ESA

Rosetta mission), the Analog Devices AD2110 will be used. Figure 3.8.1 shows the DPU block - diagram. The DPU mass is 1.0 kg and the power consumption 0.9 W.

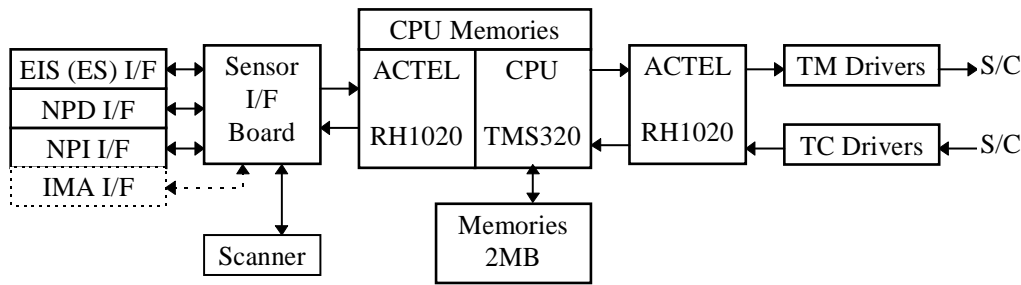


Figure 3.8.1. Block - diagram of the digital processing unit.

3.9 Operating and TM Modes

3.9.1 Operating Modes and Time Resolutions

The ASPERA-3 operation approach follows the one developed for the ASPERA-C / Mars - 96 experiment. The current operational configuration including scanning platform modes, operational sensors, voltage references, raw data accumulation period etc. is given by a single controlling word. The pre-selected sequences of the controlling words are stored in the instrument EEPROM. Each of $128 \times 8 = 1024$ entries is time - tagged and also contains the execution duration. The content of each word can be re - programmed by a command. Any word (operation configuration) or a sequence of words can be initiated by a command. This approach provides extremely high flexibility of the sensor operations.

The scanning platform has three operational modes: scanning mode, stepping mode, and fixed position mode. In the scanning mode, the platform performs scans with three pre-selected speeds 32, 64, and 128 sec in one $0^\circ - 180^\circ$ scan. In the stepping mode the platform moves in steps through the angle defined by a command. The time the platform rests in each position is also commanded. In the fixed position mode the platform moves to any position from 0° to 180° and rests there until the mode changes. The scanning platform operating modes determine the instrument internal time resolutions listed in Table 3.9.1.

Table 3.9.1. The ASPERA-3 time resolutions

Sensor	Scanning mode	Stepping mode	Fixed position
<i>Baseline</i>			
NPI	image / 32, 64, 128 s	commanded	2D ENA distribution / 62.5 ms
NPD	image / 32, 64, 128 s	commanded	2D ENA distribution / 62.5 ms
EIS	3D distribution / 32, 64, 128 s	commanded	2D ion distribution / 3s 2D electron distribution / 1s
<i>Optional</i>			
IMA	3D distribution / 32, 64, 128 s	commanded	2D ion distribution / 3s
ELS	3D distribution / 32, 64, 128 s	commanded	2D electron distribution / 1s

3.9.2 Raw Data and TM Modes

The raw data in 16 bit words are accumulated from the NPD and NPI sensors during 62.5 ms and from the EIS, ELS, IMA (design option) during 31.25 ms. The raw bit rates are given in Table 3.9.2.

Table 3.9.2. The ASPERA-3 raw data bit rates

Sensor	Raw data	Bit rate, kbits/s
<i>Baseline</i>		
NPI	$6A \times 8M \times 16E \times 16\text{bits}$	192
NPD	$32A \times 16\text{bits}$	8
EIS	$2 \times 16A \times 16\text{bits}$	16
<i>Optional</i>		
IMA	$16A \times 32M \times 16\text{bits}$	256
ELS	$16A \times 16\text{bits}$	8

A - azimuth directions, M - mass, E - energy

The raw data are pre-processed according to the current controlling word and compressed using the USES algorithm (Universal Source Encoding for Space, CCSDS 111.0-W-2). The estimated compression factor for the ASPERA-3 type of data after pre-processing is 5 - 10. The data from IMA will be reduced to approximately 1 kbyte/s by the use of look-up tables which convert the 32 mass channels to a physical mass, for example H^+ , He^{++} , He^+ , O^+ , O_2^+ .

The operating sequences will be constructed in a such way to provide three TM modes:

<i>High TM mode</i>	20 Mbytes/orbit
<i>Normal TM mode</i>	7 Mbytes/orbit
<i>Low TM mode</i>	2 Mbytes/orbit

The maximum bit rate in each TM mode does not exceed 1 Mbit/s according to the standard MIL-STD-1553.

3.10 Instrument Accommodation on the Spacecraft

Figure 3.1.1 shows the fields of view of the ASPERA-3 sensors, the scan direction, and the unit reference frame (URF). The instrument accommodation requirements listed in the priority order are:

- (1) The spacecraft shadowing of the sensor apertures must be minimized during the instrument scan;
- (2) The URF +X axis looks towards the nadir direction;
- (3) The periods when the Sun direction is within 100° of the URF +X axis must be minimized.
- (4) The instrument is located as far as possible from the ACS and orbit maneuver thrusters.

The IMA sensor (design option) should be accommodated in such a way as to provide (in priority order):

- (1) The Sun direction within the $360^\circ \times 90^\circ$ field-of-view during as long a period of each orbit as possible.
- (2) As large unobstructed field-of-view for the $360^\circ \times 90^\circ$ aperture as possible.
- (3) If possible, co-alignment between the IMA X axis and the ASPERA-3 scan platform X axis. Note, co-alignment between +X and -X axes of the units is acceptable.
- (4) Preferably, the ASPERA-3 scanner unit and IMA should be accommodated as close as possible to each other.

3.11 System Reliability and Redundancy

IRF and all other groups with hardware responsibilities have long experience with all critical components which are utilized in the ASPERA-3 experiment. We have followed a basically conservative design philosophy and have chosen whenever possible inherently reliable designs and space proven components. The NPI sensor has been flight proven and the scanner has been flight qualified for the Mars-96 mission. An instrument identical to the EIS sensor, MEDUSA, will be launched on two spacecraft Astrid-2 and Munin in 1998 and 1999. The only unit with no flight experience is the NPD sensor although all components to be used in the sensor are space proven. The two independent ENA sensors using different operational principles provide extra redundancy on the experiment level. In the case either of them fails, the instrument will still be able to fulfill the main

scientific objective and perform ENA imaging of the solar wind - atmosphere interaction. We have also been careful to ensure that no single failure of any of the major components in the instrument will disable the sensors. In addition, various backup operational sequences will be stored in the instrument DPU to bypass the possible failure.

The critical components of the experiment are the mechanical scanner, high voltage supplies, the MCP detectors, and DPU. To ensure redundant performance, the mechanical scanner will have a redundant motor and redundant drive electronic circuitry. This system developed for the Mars 96 mission requires only minor modifications to make it suitable for the Mars Express mission. Even in the case of scanner failure, the instrument is able to perform ENA imaging using the relative motion of the spacecraft with respect to the ENA generating region.

In the present design no redundancy of the high voltage supplies is foreseen. However, the HV voltage distribution between sub-systems, e.g., the deflection system plates and MCP assemblies, will be made in such a way as to guarantee ENA sensor operation with only small degradation (fewer azimuth directions or lower cut-off energies of the deflectors) in the case of a single failure. A similar approach is utilized in the EIS and IMA designs as well.

The large number (4 and 6) of MCP detectors used in parallel in the NPD provide inherent redundancy. In the case of a single failure, the sensor will suffer only a small degradation (fewer azimuth directions or lower sensitivity). For the NPI, EIS, ELS, and IMA (design option), the routing of the preamplifier inputs will be made to ensure redundancy of the sensors scientific performance.

The DPU will have fully redundant boot sequence from EEPROM and PROM, but will only incorporate one CPU circuit and one set of CPU RAM.

4. Data Reduction and Scientific Analysis Plans

The ASPERA-3 EGSE will be located at the Mars Express Operation Center (MESOC) during the mission. The EGSE will be able to decommutate raw telemetry and present both experiment housekeeping and scientific data. It will serve as the data analysis workstation during the experiment commissioning period. Once in Mars orbit, it is expected that the raw scientific data from the ASPERA-3 experiment will be delivered via Internet from MESOC to IRF and SwRI where they will be reduced, archived and further distributed to the other Co-I groups. For the correct evaluation of the imaging data provided by NPD and NPI, it is essential to receive the spacecraft auxiliary data (orbit, attitude) simultaneously with the raw data.

The reduced scientific data and the spacecraft auxiliary data will be merged and stored in a format (TBD) agreed upon by all Co-I groups. In parallel, SwRI will translate the raw data into Instrument Data File Set (IDFS) format. According to this format, physical instruments will be broken into logical (or virtual) instruments for ease in data reduction and handling. The processed IDFS data will be archived both at IRF and SwRI. The IDFS data will be made available to Co-Is immediately after processing into IDFS format. SwRI will also provide Web - based displays which will work with the reduced IDFS data, so that the data can be displayed as quickly as possible on the World Wide Web. As requested by AO, within six months after acquisition, all ASPERA-3 IDFS data will be made available to the scientific community and the public over the World Wide Web.

Co-investigators will have the option of archiving small amounts of data which are important for their current study on their local systems or requesting large data sets from an archive site. In this way, data will be transferred to the co-investigator site from the most convenient of the two archive sites. Additionally, all Co-I groups will receive the data sets in the common format.

ENA images constitute a special type of data and therefore require additional highly specialized software for scientific analysis. The raw images will reveal useful phenomenological patterns without further quantitative analysis, but only to the trained eye. The analysis programs required for producing comprehensible ENA images must be able to convert the time-series data into two and three-dimensional spatial images. Subroutines must perform a variety tasks on the raw images, such as topological transformations, motion compensation, smoothing, etc. Once the images are properly

conditioned, then algorithms can be applied to extract the global ion distributions which are the desired scientific product. Such extensive algorithms will incorporate both the parametrized models of the ion and neutral vector and scalar fields (for example, the one developed by *Kallio*, 1997), and minimizing algorithms (Section 1.9). Therefore, we foresee that the specialized programs for the ENA data analysis will be developed according to the needs of the investigations carried out at the co-investigator institutions. The resulting scientific data products (ion distributions extracted from the ENA images) will be posted on the World Wide Web in a timely manner following the posting of the ENA images that will accompany the IDFS data.

An essential element of the quantitative interpretation of the ENA images are the energy dependable instrument response functions. They will be defined during pre-flight calibrations and further verified during in-flight calibrations and inter-calibrations between NPI, NPD, and EIS (IMA in the optional configuration). IRF together with the other Co-I groups will after checking the instrument performance establish final conversion functions which will be built-in in the analyzing software.

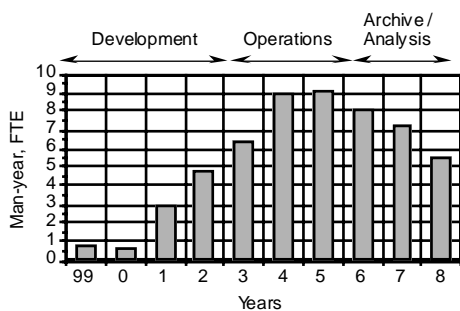


Figure 5.1. Total man-power in FTE (Full Time Equivalents) allocated for data reduction and scientific analysis.

All Co-I groups have ample experience in the analysis of large amounts of data from space missions; in particular, IRF, APL, IFSI, UA possess unique experience in working with ENA data and developing software for ENA image interpretation. Moreover, IRF, FMI, SSL, and IKI groups have been working on Martian plasma data since the Phobos mission. The Management Plan and Funding proposal give a detailed description of the available resources and equipment for the data reduction and scientific analysis. Diagram 5.1 summarizes total man-power in FTE (Full Time Equivalents) for all of the Co-I groups involved with this part of the program during all phases of the project.

5. Test and Calibration Plan

Verification of instrument function will be made both via developing and analyzing the instrument mathematical models and via intensive tests. Verification by test will be the principal method of verification. Mechanical and EMC verification and validation will be done by test. Preliminary tests will be done on circuit and board level and verification tests will be performed on instrument level. The ASPERA-3 instrument will be available for all applicable verification tests on the satellite level. Table 5.1 gives the general experiment test matrix. Calibration on the sensors level will be performed at IRF, MPAe, SwRI, and, possibly, IFSI. IKI and UA will be responsible for the tests during the development of the NPD START and STOP surfaces.

IRF has two vacuum chambers (diameter up to 1.5 m) large enough to accommodate the separate sensors and the entire instrument. They are equipped with ions sources with energies of 0.4 - 25 keV and 0.02 - 50 keV which provide large diameter (10 cm) parallel beams of a selected energy and mass and variable intensity. For the functional tests of the ENA sensors the neutral components of the ion beams will be used (see details in *Barabash*, 1995c). For the final calibrations one of the chambers will be equipped with a charge - exchanger. Two stabilized electron beam sources with energy ranges 0.5 - 70 keV and 0.1 - 100 keV (in operation at the end 1998) will also be used for the EIS calibrations and the NPI and NPD deflector system calibrations. The chambers are also equipped with the turn-tables having three degree of freedom. IRF also has numerous vacuum tanks for the storage and development of the instrument detectors.

The low energy particle accelerator at MPAe will also serve as a back-up calibration facility for the ASPERA-3 instruments. The accelerator provides a flux stabilized beam of 10^6 particles/cm² over an energy range of 20 eV to 20 keV. The beam area is up to 10 cm².

IKI chamber with a rotational turn-table (two degrees of freedom), ion beam in the energy range 0.03 - 25 keV and equipped with an MCP position - sensitive detector is well suited for the analysis of the START surface reflection properties.

To perform the laboratory studies of the optical properties of the START and STOP surfaces, i.e. reflectivity of UV and production of photo-electrons, we will use the EUV and FUV facility at the Lunar and Planetary Laboratory of the University of Arizona (UA). This facility is housed in a class-100K room and equipped with a four-axis gimbals system. EUV light is derived from flow-through sources, either a microwave-excited discharge or a DC glow discharge. The light is dispersed and collimated by a modified Seya-Namioka monochromator. This calibration facility has been used for the test and calibration of a number of UV spectrometers (starting from Mariner 10) and conducting transmission measurements for thin foils intended for use in ENA instruments. An electron detector will be installed for the proposed study of photoelectron yields.

An extensive check-out program after the first turn-on of the instrument is foreseen . The function of the DPU and the sensor electronics will routinely be monitored throughout the mission by the check-out software within the DPU. In flight, the NPI and NPD will be inter - calibrated with each other. In addition, by turning off the deflector high voltage, the NPD sensor can be inter - calibrated with the EIS sensors and / or a mass spectrometer, e.g., IMA in the design option. The NPI, NPD, EIS (IMA) inter - calibrations will be performed routinely to verify the stability of the conversion surfaces of the ENA imagers.

Table 5.1. The general experiment test matrix

Activity	SM	ELM	FM	Responsibilities
Mechanical Interface, Mass Inspection	M	-	M	IRF
Electrical Performance	-	M	M	IRF, FMI, IFSI, MPAe, SwRI
Functional Test	-	F	F	IRF, FMI, IFSI, MPAe, SwRI
Strength Test	M	-	M	Swedish Industry
Sine and Random Vibrations, Shock Test	Q	-	A	Swedish Industry
Thermal Balance Test	-	-	-	IRF Solar simulator
Thermal Vacuum Test	-	-	A	IRF Thermal vacuum tank
EMC Conducted & Radiated	-	-	Q/A	Swedish Industry
Sensor Calibration	-	-	C	IRF, MPAe, IKI, UA, IFSI
DC Magnetic Test	-	-	-	IRF, Swedish Industry

A - Acceptance Test, C - Calibration, F - Functional test, M - Inspection/Measurement, Q - Qualification Test

6. System Level Assembly, Integration and Verification

The ASPERA-3 instrument could preferably be attached with six mounting screws (i.e. M4-M5 screws/bolts, Titanium or Stainless Steel). No mechanical ground support equipment is required to mount or handle the ASPERA-3 instrument. The only constraints on the ground handling of the ASPERA-3 instrument is to maintain contamination control in the area around the instrument when it is out of its shipping container. A class 100K clean room is adequate for exposure of the instrument to room air. A slow purge of GN2 (99.99%) should be maintained through the instrument whenever it is not stored in its shipping container. A purging system adapter (a standard ESA purging interface through a Swagelok tube male fitting) will be available on the instrument.

A major part of the instrument could (and preferably should) be covered in multiple-layer isolation (not included in mass calculation so far). The ASPERA-3 instrument could be thermally isolated by inserting thermoplastic mounting brackets between the preferred six mounting attachment points. After the mounting position has been decided for the ASPERA-3 instrument and thermal analysis and preliminary thermal tests have been performed a decision has to be made as to whether

the ASPERA-3 instrument needs a non-op heater. At this stage a maximum 2.0 W heater budget should be reserved for the ASPERA-3 instrument.

The model philosophy of the ASPERA-3 instrument will ensure that the satellite system prime contractor will have an applicable model of the instrument throughout all stages of the project. The ASPERA-3 models and deliverable items will be: Structural Model (SM), Electrical Model (ELM) and Flight Model (FM).

7. Flight Operations

The pre-selected sequences stored on-board (Section 3.8) include various combinations of the mode changes required for effective data collection. The sequences can be initiated by a single command or another internal sequence. This makes the flight operation simple and flexible and significantly reduces the number of commands to be sent. During normal operation at Mars and cruise - phase calibrations the instrument does not require more than 5 - 8 commands per orbit / session to be initiated. The commissioning phase requires around 10 command per session.

The instrument contains high voltages up to (5 kV) and thus the initial turn-on must be conducted not earlier than two weeks after the launch.

During the cruise phase it would be desirable, although not mandatory, to turn on the instrument for a few days every week to perform calibrations in the undisturbed solar wind and attempt performing measurements of the interstellar wind. The later opportunity is particularly important because that would allow one to correlate these observations with the measurements of the GAS instrument on the ESA spacecraft ULYSSES and check the instrument performance at very low ENA energies. It is only during the cruise phase one can achieve the long integration periods needed for the interstellar gas measurements.

While approaching Mars, it is quite desirable to start scientific operations from about 50.000 km (TBC) to investigate ENA emissions at large distances. However, the instrument must be turned off during main orbital corrections (such as braking) due to the danger of high voltage break-down.

During normal operation at Mars, the instrument shall be turned on over the entire orbit in order to perform ENA imaging from all possible distances. Operation of the ACS thrusters could interface with the IMA and EIS measurements although cause no damage for the experiment (TBC).

8. Organization and Management Structure of the Instrument Team

8.1 Instrument Development

ASPERA-3 will be designed, fabricated, tested, and calibrated jointly by the proposing institutions, see the organization chart (Figure 9.1.1). IRF will be the lead institution, responsible for all sensors and the scanning platform. The responsibility of these units concentrated at IRF will ensure efficient project control and greatly improve the design, fabrication, testing, and calibration efforts. FMI will be responsible for the DPU, and IFSI for the EGSE. Vital parts of the NPD will be designed and fabricated at institutions with world-renowned experience. The time-of-flight electronics will be made by MP Ae and the MCP assemblies by RAL. The EIS sensor will be designed and fabricated by SwRI. In addition to the hardware effort described in the organization chart (Figure 9.1.1), SwRI will be responsible for developing the software for data production, analysis, and archiving.

All groups involved have a long and successful history of experience in space projects and have set up a well established management system which allows for accurate and continuous monitoring of progress and costs.

The key members of this investigation are:

Principal Investigator: Prof. Rickard Lundin, Director of the Swedish Institute of Space Physics. The PI, with experience of three previous Mars experiments (ASPERA/Phobos, ASPERA-

C/Mars-96, IMI/Planet-B), as well as numerous other PI and Co-I responsibilities, will ensure that the proposed investigation is successfully carried out in accordance within the project schedule and cost. He will supervise all experiment definition, instrument design and development, and support for mission operations. He is responsible for supplying the experiment, support equipment, documentation, and required software on time and to the agreed specifications. The ASPERA-3 PI represents the single point formal interface with the ESA Mars Express Project Office for scientific and general matters.

Co-Principal Investigator: Dr. Stanislav Barabash. The Co-PI has participated in several Mars plasma experiments (ASPERA/Phobos-1 and -2, ASPERA-C/Mars-96) as Co-I, as well as being a PI for the ENA instrument PIPPI / Astrid-1). He will assume overall responsibility for co-ordinating the ASPERA-3 development, as well as being a hardware - providing Co-I.

Experiment Manager: Mr. Joakim Gimholt. He has participated in several previous experiment development efforts, such as Freja, Astrid-1, Mars-96, Planet-B, and Rosetta. He will coordinate the hardware and software efforts of all segments of ASPERA-3, and interface with the responsible engineers at the Co-I institutions. The Experiment Manager represents the single point formal interface with the ESA Mars Express Project Office for technical matters.

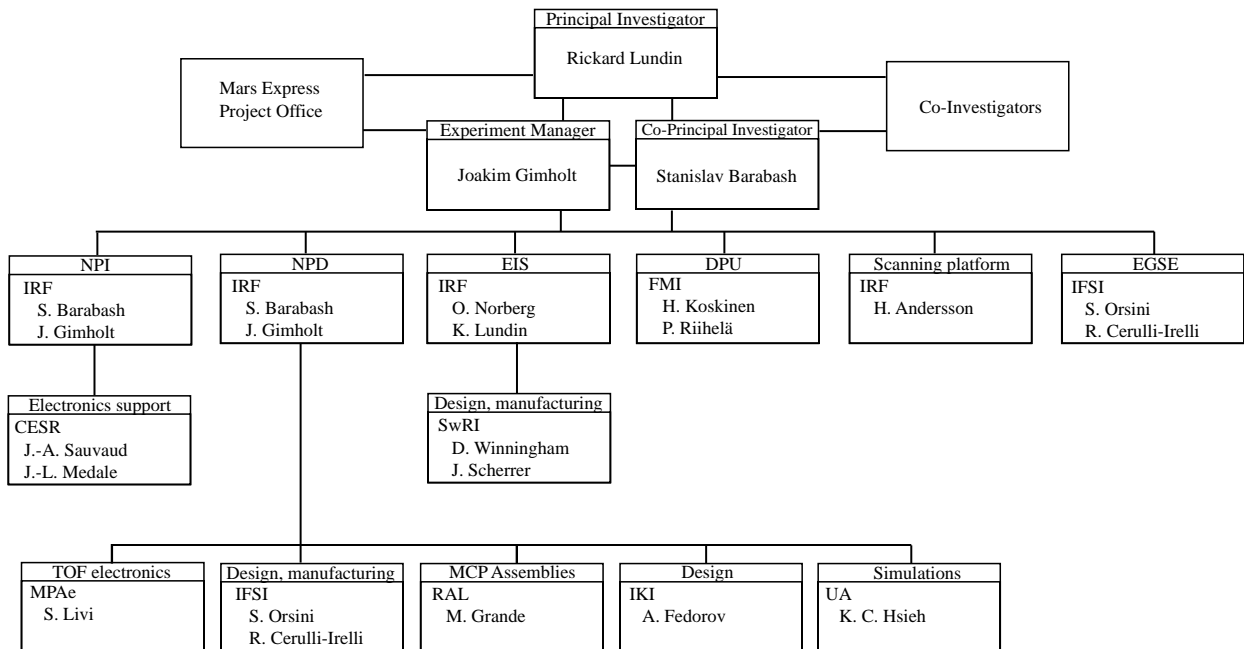


Figure 9.1.1. Functional organizational chart of the ASPERA-3 instrument development.

8.2 Science Operations

For the science operation activities we propose to form the ASPERA-3 Science Operation Group (ASOG). ASOG will include PI, EM, Co-PI, the leading Co-Is responsible for the sensors, and a key software engineer responsible for the data reduction and archiving. In the close connection with Mars Express Operation Center (MESOC), ASOG will perform the instrument operation and commanding scheduling, evaluation of the housekeeping information, and analysis of the raw scientific data. ASOG will also be responsible for the data reduction, archiving, and distribution to the other Co-I groups. During the commissioning phase and the other crucial mission periods, e.g., beginning of the instrument operation at Mars, ASOG can be situated at ESOC or wherever the ASPERA-3 EGSE de - communicating the raw telemetry is placed. Normally, ASOG is located at IRF communicating with MESOC and Co-I groups via Internet even in real time.

9. Description of the Instrument Team Qualifications and Experience

9.1 Scientific Personnel

Rickard Lundin (IRF, Principal Investigator), Director of the Swedish Institute of Space Physics; Professor in Space Physics at the University of Umeå (1989). Experience: PI for the ion composition experiment PROMICS/Prognoz-7, 8, the hot plasma experiment on Viking, the mass spectrometer ASPERA/PHOBOS, and the hot plasma and ENA experiment ASPERA-C/Mars-96, the mass spectrometers IMI/Planet-B, and ICA/Rosetta. PI for about ten hot plasma experiments using the sounding rockets. Project Scientist for the Swedish Freja satellite. Co-I on hot plasma experiments for Freja, Equator-S, Cluster.

Stanislav Barabash (IRF), Scientist at the Swedish Institute of Space Physics, Kiruna; PhD in Space Physics at the Swedish Institute of Space Physics, Kiruna (1996). Experience: Instrument design, data analysis, and theory. Co-I on the ASPERA / Phobos (data analysis), ASPERA-C / Mars-96 (design, development, and calibration of the ENA sensors), PROMICS-3 / Interball - Auroral, - Tail (development, calibrations). PI for the ENA imager PIPPI / Astrid-1 and the ENA detector DINA / nanosatellite Munin.

Riccardo Cerulli-Irelli (IFSI), Research staff member at the Italian Research Council Istituto di Fisica dello Spazio Interplanetario; 'Laurea' in physics at the Rome University (1967). Experience: plasma experiments HEOS-2 / S-202 (tests, management), EGD/ISEE-2 (project manager), plasma composition experiment for the NASA cometary mission (design), plasma composition experiment JPA/Giotto (project manager), ISO/LWS-DPU (digital electronics design), Equator-S / CIS (management and design), SAC-B/ISENA (project manager), TSS-1R/RENE (team member).

Charles Curtis (UA), Research Associate Professor at the University of Arizona; PhD in Physics, University of Arizona (1978). Experience: Designer of FIS (Field Ionization mass Spectrometer) and EIS (Electron Impact mass Spectrometer) sensors for the VEGA probes to Comet Halley. Project manager for the development of the EUV Imager for NASA's IMAGE Mission.

Andrei Fedorov (IKI), Senior Scientist at Space Research Institute (IKI), Moscow; M.Sc. in Experimental Nuclear Physics from Moscow Institute of Physics and Technology (1980). Experience: Design, simulation, development, and calibration of plasma instrumentation. Data analysis and data analysis software. Design and development of the calibration facility. PI for the ion spectrometers TRIPLET, VDP/Interball. Leading Co-I on the plasma analyzers BIFRAM/Intershock, CORALL/Interball, FONEMA / Mars-96, and ENA detector DINA / Swedish nanosatellite Munin.

Rudy Frahm (SwRI), Research Scientist at Southwest Research Institute, San Antonio, Texas; PhD in Space Physics and Astronomy, Rice University (1987). Experience: Design, development, calibration, and flight operations of electron and ions instruments on UARS/MEPS, TSS/SPES, DMSP / SSJ/4, and numerous sounding rockets.

Manuel Grande (RAL), Leader of Experimental Solar System Physics Group at Rutherford Appleton Laboratory; PhD in Cosmic Ray Physics at Bristol University (1986). Experience: Deputy PI in RAPID/Cluster, and Co-I in CAPS/Cassini, PEACE/Cluster, Cammice/GGS/POLAR. Co-I and hardware contributor to a number of recent ENA Imaging Missions, including GGS / POLAR Ceppad, ISENA / SAC-B, MENA / IMAGE mission.

Ke Chiang Hsieh (UA), Professor at the University of Arizona, Tucson; PhD in Physics at University of Chicago (1969). Experience: Development of energetic neutral atom detectors and imagers since 1979. PI for the neutral gas mass analyzers for Soviet VEGA mission to Comet Halley. Original instrument lead of the High Energy Neutral Atom imager for NASA's IMAGE Mission. Co-I on CELIAS/SOHO, MIMI/Cassini, and HENA/IMAGE .

Esa Kallio (FMI), Scientist at the Geophysical Research Division of the Finnish Meteorological Institute. PhD degree in 1996 with a thesis titled "Mars-Solar Wind Interaction: Ion Observations and their Interpretation". Experience: Data analysis of the mass spectrometer Phobos/ASPERA, analysis of ENA production at Mars.

Hannu Koskinen (FMI), Professor in Space Physics, University of Helsinki. (also at the Finnish Meteorological Institute, Geophysical Research); PhD at the Swedish Institute of Space Physics, Uppsala (1985). Experience: data analysis of ion mass spectrometer Phobos/ASPERA, Co-I on ion and ENA spectrometer Mars-96/ASPERA-C (leader of the FMI participation, DPU H/W and S/W); Co-I on ENA imager Astrid-1/PIPII.

Janet Kozyra (SPRL), Associate Research Scientist at Space Physics Research Laboratory, University of Michigan; PhD in Atmospheric Sciences, University of Michigan (1986). Experience: Theory and modelling of the ionosphere - magnetosphere coupling processes. Participation in the data analysis in the DE, AMPTE/CCE programs. Interdisciplinary Scientist in the Thermosphere - Ionosphere - Mesosphere Energetic and Dynamics (TIMED) mission. Specific research areas include, within others, neutral atom and ion precipitation, and loss model for ring current decay.

Norbert Krupp (MPAe), Scientific Staff member at Max-Planck-Institut für Aeronomie, Katlenburg-Lindau; PhD at Technical University Braunschweig, Institute of Geophysics and Meteorology, (1994). Experience: Scientific analysis and interpretation of particle and magnetometer data from ULYSSES and GALILEO. Science team member of the MIMI instrument on CASSINI.

Stefano Livi (MPAe), Scientific Staff member, Max-Planck-Institut für Aeronomie, Katlenburg-Lindau, Germany; University of Florence, PhD (1982). Experience: Co-PI of the ion composition experiment CAMMICE on POLAR, the magnetospheric imaging instrument MIMI on CASSINI, leading Co-I on the TOF-mass spectrometer RTOF/ROSINA on ROSETTA, Co-I on in situ and remote sensing of plasmas on the AMPTE, PHOBOS, CRRES, GALILEO, ULYSSES, GEOTAIL, SOHO, POLAR, CLUSTER 2 GIOTTO mission. Scientific analysis of in-situ ion composition and energetic ion data.

Janet Luhmann (SSL), Senior Fellow at Space Sciences Laboratory, University of California in Berkeley; PhD in Astronomy, the University of Maryland (1974). Experience: Theory, modelling, data analysis concentrated on the solar wind interaction with the weakly magnetized planets, Venus and Mars. Responsible for Pioneer Venus magnetometer data analysis. Co-I on two POLAR experiments, and a member of the ion-neutral mass spectrometer facility instrument team on Cassini.

Olle Norberg (IRF), Scientist at the Swedish Institute of Space Physics, Kiruna.; M.Sc. in Engineering Physics at the Royal Institute of Technology, Stockholm (1988). Experience: Co-I on Phobos, Freja, Mars-96, and Planet-B. Project Scientist and PI on Astrid-1 and Munin, PI on Astrid-2, Co-PI on the Ion Composition Analyzer on Rosetta. Experienced in managing large collaborative projects, and design and calibration of plasma analyzers.

Stefano Orsini (IFSI), Research staff member at the Italian Research Council Istituto di Fisica dello Spazio Interplanetario (ricercatore); 'Laurea' in physics at the University of Rome(1976) Experience: Co-I on plasma experiments ISEE-2/EGD (scientific data analysis), INTERBALL / OPERA (software, EGSE), TSS-1, TSS-1R / TEMAC; PI of the ENA instrument ISENA/SAC-B.

Edmond Roelof (APL), Principal Professional Staff , The Johns Hopkins University Applied Physics Laboratory; PhD, University of California, Berkeley, (1966). Experience: Theory and analysis of data on energetic charged particles and ENA imaging. Co-I on Pioneer 10/11: Cosmic Ray Energy Spectra Experiment, Galileo / EPD, Ulysses / SPECAM, Geotail /EPIC, Cassini / INCA, TWINS and Astrid / Energetic neutral atom imagers.

Bill Sandel (UA), Senior Research Scientist at Lunar and Planetary Laboratory of the University of Arizona; PhD in Space Science, Rice University (1972). Experience: PI for the UV intensifiers in the Auroral Imager for Viking, and EUV Imager on IMAGE. Co-I on UVS/Voyager, UVS/EUV / Galileo. Development of advanced photon-counting array detectors for eight Shuttle experiments and an EUV-FUV telescope to study stars and the Jupiter system.

Jean-Andre Sauvaud (CESR), Director of Research at CNRS, Head of the solar system department at CESR; Docteur es Sciences from the University of Toulouse (1977). Experience: Instrument design, data analysis, and project management. Co-I on various space missions including, ARCAD 1, 2, 3, ISEE-1, 2, Giotto, Mars-96, MOM, MGS,Cluster. PI on the two Interball satellites.

James Sharber (SwRI), Staff scientist at Southwest Research Institute, San Antonio, Texas; PhD in Physics from Texas A & M University (1972). Experience: Analysis of data from rocket flights as well as the ISIS, DE., NOAA, Viking, and UARS satellites. Co-I on UARS, Cluster. PI for particle detectors on PULSAUR II, four ARIA (Atmospheric Response In Aurora) campaigns and those being built for the Svalbard Cusp Transient Features Campaign to be launched late in 1997.

Donald Williams (APL), Chief Scientist at Milton S. Eisenhower Research Center, Applied Physics Laboratory, The Johns Hopkins University; PhD, Yale University (1961). Experience: PI and Co-Investigator on large number of NASA, NOAA, DoD and European research and operational satellites, including: PI on Galileo /EPD and Geotail / EPIC particle detectors.

David Winningham (SwRI), Scientist at Southwest Research Institute, San Antonio, Texas; PhD in Physics from Texas A & M University (1970); Experience: PI for the plasma instruments on DE-2, PEM/UARS, plasma analyzers on Giotto, TSS-1, TSS-1R, and numerous sounding rockets. Co-I on electron and ion spectrometers for ISIS-1/2, DE-1, and numerous sounding rockets. PI on AFGL data analysis contracts. His responsibilities in all of these programs have included instrument development and data analysis.

Joachim Woch (MPAe), Scientific Staff member at Max-Planck-Institut für Aeronomie, Katlenburg-Lindau; PhD at University of Göttingen, Institute of Geophysics, (1987). Experience: Co-I on the experiments SWICS and EPAC on ULYSSES, PROMICS on Interball, RAPID on Cluster 2 and ROSINA on Rosetta. Scientific data analysis and interpretation of particle and magnetometer data from GEOS, Viking, Ulysses, Polar and Galileo.

Masatoshi Yamauchi (IRF), Scientific Staff at Swedish Institute of Space Physics, Kiruna; PhD in Space Physics from University of Alaska, Fairbanks (1990). Experience: Analysis of data from Magsat, Viking, Freja, and Ulysses spacecraft. Co-I for IMI instrument for Planet-B spacecraft (test and calibration). Analytical theories and MHD numerical simulation.

9.2 Key Technical Personnel

Joakim Gimholt (IRF, Experiment Manager), Project Manager and R&D Engineer at the Swedish Institute of Space Physics; M.Sc. in Computer Science and Engineering, Luleå Technical University, 1991. Experience: Electronics and mechanics design, vacuum and cryogenic technology, particle detector development/design/testing, and project management. Leading electrical engineer of ASPERA-C/Mars-96, IMIS/Planet-B, IMI/Freja, PIPPI/Astrid-1, MEDUSA/ Astrid-2. Quality Assurance Manager for the ICA/Rosetta. Overall management of the thermal - vacuum and calibration facilities at IRF and test coordination for Astrid, Freja, and Cassini (sub-units).

Kjell Lundin (IRF), Head of the electronics group at the Swedish Institute of Space Physics, Kiruna; Experience: Space plasma instruments (all aspects), project management. More than 25 years experience in space projects starting from ESRO-4. At the present, Technical Manager of the ICA experiment for the ESA Rosetta mission.

Herman Andersson (IRF), Senior research engineer at the Swedish Institute of Space Physics. Experience: development, design and testing of particle detecting instruments and ground support equipment, including design of electronics and mechanical systems, project management. Participated as lead electrical engineer, project assurance manager or experiment manager in satellite projects such as Interball-1&2&3, Viking, Phobos-1&2, Freja, Mars-96 and Rosetta and national sounding rocket projects.

Pekka Riihelä (FMI), Design engineer at the Finnish Meteorological Institute. Experience: Digital electronics design. Participation in the projects Phobos/ASPERA (Memory Unit), Interball/PROMICS-3 (Part of DPU electronics), Mars-96/ASPERA-C (DPU), SOHO/SWAN (part of DPU), Astrid-1: (Data Compression Unit), Rosetta/ICA&LAP (DPU), Rosetta Lander / CDMS (Memory Unit).

Jouni Rynö (FMI), Design engineer at the Finnish Meteorological Institute; M.Sc. Experience: Flight software development, data compression. Participation in the projects Mars-96 / ASPERA-C

(design, coding, and tests of flight software), Astrid-1 (data compression software, Stardust / CIDA (flight software)).

John Scherrer (SwRI), Group Leader at Southwest Research Institute, San Antonio, Texas; MBA, University of Texas at San Antonio, 1986. Experience: Electronics packaging, vacuum technology, particle detector design and testing. Participation in programs UARS, GGS, SEPAC, TSS, Wakeshield and Comet. Leading mechanical engineer and project manager for plasma particle detectors including MAIMIK SPI, Polar ARCS AREA, ARIA SPS, the CENTAUR sounding rocket payloads. Project manager and mechanical engineer of the analyzer MEDUSA for Astrid-2.

Carrie Gonzalez (SwRI), Senior Research Analyst at Southwest Research Institute, San Antonio, Texas; M.Sc. in Industrial Engineering, St. Mary's University, 1989. Experience: Scientific software development. Primary author of science data analysis systems for the DE and Giotto particle instruments, for the Science Operations Center (SOC) for the Tethered Satellite System. Primary author of data handling routing for the SDDAS system developed by SwRI.

Jean-Louis Medale (CESR), Engineer at Centre d'Etude Spatiale des Rayonnements. Experience: Particle detectors and related analog electronics, TOF electronics, MCP imaging systems. Projects: ARCAD-3, Giotto, MSG, Cluster, Equator-S.

Donald Reading (RAL), Senior Scientific Officer in the space science department at Rutherford Appleton Laboratory; PhD in High Energy Physics at University. Experience: Long career as instrument physicist on numerous space and high energy experiments. Responsible for Cluster MCP testing at RAL and UV rejection filter testing for IMAGE/MENA and SAC-B/ISENA.

Elena Budnick (IKI), Research staff at the Space Research Institute, Moscow; M. Sc. Moscow State University, 1977. Experience: Scientific software development and data analysis. Co-I on the PROMICS-3 mass spectrometer and SKA-2/Interball, and ASPERA-C/Mars - 96. Participation in the IKI-DD system development. Data analysis software for the high-energy detectors for PROGNOZ-7 and PROGNOZ-8 spacecraft.

9.3 Relevant Publications

- Barabash S., et al., Energetic neutral atom imager on the Swedish microsatellite Astrid, in *Measurement Techniques in Space Plasma*, AGU monograph, in press, 1998.
- Barabash S., et al., Energetic neutral atom imaging by the Astrid microsatellite, *Adv. Space Res.*, 20, 1055, 1997.
- Barabash S., et al., Diagnostic of energetic neutral particles at Mars by the ASPERA-C instrument for the Mars 94 mission, *Adv. Space Res.*, 16, (4)81, 1995
- Barabash S., E. Kallio, R. Lundin, H. Koskinen, Measurements of nonthermal helium escape from Mars, *J. Geophys. Res.*, 100, 21,307, 1995.
- Beutier, T., J.-A. Sauvaud, et al., Global Imaging by Energetic Neutral Particles, in *Radiation Belts Models and Standards*, AGU Geophysical Monograph 97, p.281, 1997
- Blake, J. B. et al., including M. Grande, Comprehensive Energetic Particle and Pitch Angle Distribution Experiment on POLAR, *Space Science Review*, 71, 1995.
- Curtis, C., and K. C. Hsieh, Remote sensing of planetary magnetospheres: Imaging via energetic neutral atoms, in *Solar System Plasma Physics*, eds. J. H. Waite, Jr., J. L. Burch, and R. L. Moore, Geophysical Monograph Series, Vol. 54, 247, 1989.
- Frahm, R. A., J. D. Winningham, J. R. Sharber, et al., The diffuse aurora: a significant source of ionization in the middle atmosphere, *J. Geophys. Res.*, 102, 28203, 1997.
- Fedorov, A., et. al., The method of non-scanning measurements of ion distribution function realised in two Instruments for INTERBALL and MARS-96 projects, in *Measurement Techniques in Space Plasma*, AGU monograph, in press, 1998.
- Grande M., Investigations of Magnetospheric Interactions with the Hermean Surface *Adv. Space Res.* 19, 1609, 1997.
- Herbert, F., and B. R. Sandel, Radial profiles of ion density and parallel temperature in the Io plasma torus during the Voyager 1 encounter, *J. Geophys. Res.*, 100, 19513, 1995.
- Hsieh, K. C., and C. C. Curtis, A model for the spatial and energy distributions of energetic neutral atoms produced within the Saturn/Titan plasma system, *Geophys. res. Lett.*, 15, 772, 1988.
- Hsieh, K. C. , et al., H Lyman alpha transmittance of thin C and Si/C foils for keV particle detectors, *Nucl. Instr. Meth. B61*, 187, 1991.
- Johnstone, A., et al. including J. D. Winningham, Ion Flow at Comet Halley, *Nature*, 321, 344, 1986.
- Kallio E., et al., Charge - exchange near Mars: the solar wind absorption and energetic neutral atom production, *J. Geophys. Res.*, 102, 22,183, 1997.
- Kallio E. et al., Proton flow in the Martian Magnetosheath, *J. Geophys. Res.*, 99, 23547, 1994.
- Kallio E., An empirical model of the solar wind flow around Mars, *J. Geophys. Res.*, 101, 11,133, 1996.
- Kallio E., H. Koskinen, et al., Oxygen outflow in the Martian magnetotail, *Geophys. Res. Lett.*, 22, 2449, 1995.
- Kallio E., H. Koskinen, et al., 3D Plasma Observations near Mars, *Geophys. Res. Lett.*, 20, 2339, 1993.
- Kozyra, J. U., et al., Energetic O⁺ Precipitation, *J. Geophys. Res.*, 87, 2481, 1982.
- Kozyra J. U., et al., The role of ring current O⁺ in the formation of stable auroral red arcs, *J. Geophys. Res.*, 92, 7487, 1987.

- Luhmann J. G. and J. U. Kozyra, Dayside pickup oxygen ion precipitation at Venus and Mars: Spatial distributions, energy deposition, and consequences, *J. Geophys. Res.*, 96, 5457, 1991.
- Luhmann, J. G. and L. H. Brace, Near-Mars Space, *Rev Geophys*, 29, 121, 1991.
- Luhmann J. G., The solar wind interaction with Venus and Mars: Cometary analogies and contrasts, in *Geophysical Monograph* 61, AGU, 5, 1991.
- Luhmann, J. G., et al., Evolutionary impact of sputtering of the Martian atmosphere by O⁺ pickup ions, *Geophys. Res. Lett.*, 19, 2151, 1992.
- Lui, A.T.Y., D.J. Williams, et al., First Composition Measurements of Energetic Neutral Atoms, *Geophys. Res. Lett.*, 23, 2641, 1996.
- Lundin, R., et al, First measurements of the ionospheric plasma escape from Mars, *Nature*, 341, 609, 1989.
- Lundin, R., et al., Plasma composition measurements of the Martian magnetosphere morphology, *Geophys. Res. Lett.*, 17, 877, 1990.
- Lundin, R., and E. Dubinin, Phobos-2 results on the ionospheric plasma escape from Mars, *Adv. Space res.*, 12, (9)255, 1992.
- Mitchell, D. G., including K. C. Hsieh, INCA: the ion neutral camera for energetic neutral atom imaging of the Saturnian magnetosphere, *Optical Engineering*, 32, 3096, 1993.
- Norberg, et al., Observations of molecular ions in the Martian plasma environment, in *Plasma environments of non-magnetized planets*, edited by T. I. Gombosi, pp. 299, Pergamon Press, Oxford, 1993.
- Norberg, O., et al., The microsatellite ASTRID, *Proceedings 12th ESA Symposium on Rocket and Balloon Programmes and Related Research*, Lillehammer, Norway, 273, 1995.
- Norberg, O., et al., The ion mass imager on the Planet-B spacecraft, *Earth Planet. Sci.*, in press, 1998.
- Orsini, S., et al. including K. C. Hsieh, Model calculation of energetic neutral atoms precipitation at low altitudes, *J. Geophys. Res.*, 99, 483, 1994.
- Orsini, S., et al. including M. Grande, Remote Sensing the Earth's Magnetosphere: an Instrument for Energetic Neutral Atoms based on Time-of-Flight and Solid State Detectors, in *Measurement Techniques in Space Plasmas*, AGU Monograph, in press, 1996.
- Roelof, E. C., Energetic neutral atom imaging of magnetospheric ions from high- and low-altitude spacecraft, *Adv. Space Res.*, 20, 341, 1997.
- Roelof, E. C., Energetic neutral atom image of a storm-time ring current, *Geophys. Res. Lett.*, 14, 652, 1987.
- Roelof, E. C., et al., Energetic neutral atoms (E~50 keV) from the ring current: IMP 7/8 and ISEE 1, *J. Geophys. Res.*, 90, 10991, 1985.
- Sandel, B., et al. including C. Curtis, Imaging extreme ultraviolet photons and energetic neutral atoms: a common approach, *Remote Sensing Review*, 8, 147, 1993.
- Sandel, B. R., Ultraviolet Spectroscopy, in *Encyclopedia of Planetary Sciences*, Van Nostrand-Reinhold, 1997.
- Semkova, Y., R. Koleva, A. Fedorov et al., Energy-mass spectrometer of angular scanning for low energy weak ion flux analysis, preprint IAF-86-292, 1986.
- Sauvaud, et al., On the origin of flux dropouts during substorm near synchronous orbit -betatron deceleration, *J. Geophys. Res.*, 101, 19911, 1996
- Sauvaud, J.-A., et al., The electron experiment onboard Interball-Tail, initial results on the low latitude boundary layer of the dawn magnetosphere, *Ann. Geophys.*, 15, 587, 1997.
- Sharber, J. R., J. D. Winningham, et al., Design, construction, and laboratory evaluation of the angle resolving energy analyzer (AREA): A "Top-Hat" instrument for auroral research, *IEEE Trans. on Geoscience and Remote Sensing*, GE-26, 474, 1988.
- Sharber, J. R., R. A. Frahm, J. D. Winningham, et al., Observations of the UARS particle environment monitor and computation of ionization rates in the middle and upper atmosphere during a geomagnetic storm, *Geophys. Res. Lett.*, 20, 1319, 1993.
- Sharber, J. R., et al., Validation of UARS particle environment monitor electron energy deposition, *J. Geophys. Res.*, 101, 9571, 1996.
- Vaisberg O., A. Fedorov, et al, The possibility of making fast measurement of ion distribution function, Proc. Int. Workshop on Space Plasma Physics Investigation by Cluster and Regatta, ESA SP-306, 143, 1990.
- Williams, D. J., E. C. Roelof, and D. G. Mitchell, Global magnetospheric imaging, *Rev. of Geoph.*, 30, 183, 1992.
- Williams, D. J., Why We Need Global Observations, in *Magnetospheric Physics*, Eds. B. Hultqvist and C.-G. Fälthammar, Plenum Press, New York, 83, 1990.
- Winningham, J. D., et al., The Low Altitude Plasma Instrument (LAPI), *Space Sci. Instrum.* 5, 465, 1981.
- Winningham, J. D., and C. N. Gurgiolo, DE-2 Photoelectron Measurements Consistent with a Large Scale Parallel Electric Field over the Polar Cap, *Geophys. Res. Lett.*, 9, 977, 1982.
- Winningham, J. D., J. R. Sharber, R. A. Frahm, et al., The UARS particle environment monitor, *J. Geophys. Res.*, 88, 10649, 1993.
- Yamauchi, M., Numerical simulation of large-scale field-aligned current generation from finite-amplitude magnetosonic waves, *Geophys. Res. Lett.*, 21, 851, 1994.
- Yamauchi, M. et al, Dynamic response of the cusp morphology to the solar wind: A case study during passage of the solar wind plasma cloud on February 21, 1994, *J. Geophys. Res.*, 101, 24,675, 1996.

References

- Acuna, M. H., et al., Mars Global Surveyor Magnetic field investigation (MAG/ER): Preliminary Results, *Eos*, 78, 400, 1997.
- Anderson, D. E., Mariner 6, 7, and 9 ultraviolet spectrometer: Analysis of hydrogen Lyman alpha data, *J. Geophys. Res.*, 79, 1513, 1974.
- Banaszkiewicz, M., and W.-H. Ip, A statistical study of impact ejecta distribution around Phobos and Deimos, *Icarus*, 90, 237, 1991.
- Barabash, S., E. Dubinin, N. Pissarenko, R. Lundin, and C. Russell, Picked up protons near Mars: PHOBOS observations, *Geophys. Res. Lett.*, 18, 1805, 1991.
- Barabash, S., and R. Lundin, On a possible dust-plasma interaction at Mars, *IEEE Trans. on plasma science*, 22, 173, 1994.
- Barabash, S., E. Kallio, R. Lundin, and H. Koskinen, Measurements of nonthermal helium escape from Mars, *J. Geophys. Res.*, 100, 21,307, 1995a.

- Barabash, S., et al., Diagnostic of energetic neutral particles at Mars by the ASPERA-C instrument for the Mars 96 mission, *Adv. Space Res.*, 16, (4)81, 1995b.
- Barabash, S., Satellite observations of the plasma - neutral coupling near Mars and the earth, *IRF Scientific Report*, 228, 1995c.
- Barabash et al., Results from ENA imaging on the microsatellite Astrid, *Eos*, 77, 565, 1996.
- Barabash, S., et al., Energetic neutral atom imager on the Swedish microsatellite Astrid, in *Measurement Techniques in Space Plasma*, AGU monograph, in press, 1998.
- Bauske, R., et al., Ionospheric storm effects in the nighttime E region caused by neutralized ring current particles, *Ann. Geophysicae*, 15, 300, 1997.
- Benazeth, N., Review on kinetic ion-electron emission from solid metallic targets, *Nucl. Instr. and Meth.*, 194, 405, 1982.
- Brecht, S.H., Solar Wind proton deposition into the Martian atmosphere, *J. Geophys. Res.* 102, 11,287, 1997.
- Burch, J. L., Imager for Magnetopause - to - Aurora Global Exploration (IMAGE), *A proposal to NASA*, June, 1995.
- Chamres, E. S., Secondary-electron yield on copper-beryllium for H^+ , H_2^+ , H_3^+ , H^0 , H_2^0 , and H_3^0 , *Phys. Rev.*, 133, A1202, 1964.
- Coggiola, M. J., Secondary electron yields from Mo and Mo/Cs surfaces by ion impact, *Nucl. Instrum. Methods*, B13, 641, 1986.
- Dementyeva, N., et al., Preliminary results of measurements of UV emissions scattered in the Martian upper atmosphere, *Icarus*, 17, 475, 1972.
- Dostovalov, S. B., and S. D. Chuvahin, Distribution of neutral hydrogen in the Martian upper atmosphere, *Cosmic. res.*, 11, Engl. Transl., 767, 1973.
- Dornheim, M. A., Mars atmosphere thicker than expected, *Aviation Week and Technology*, September 29, 36, 1997.
- Dubinin, E., et al., Plasma characteristics of the boundary layer in the Martian magnetosphere, *J. Geophys. Res.*, 101, 27,061, 1996.
- Farmer, C. B., et al., Mars: Water vapour observations from the Viking orbiters, *J. Geophys. Res.*, 82, 4225, 1977.
- Funsten, H. O., et al., Comparative study of low-energy neutral atom imaging techniques, *Optical Engineering*, 33(2), 349, 1994.
- Grard, R. J. L., Properties of the satellite photoelectron sheath derived from photoemission laboratory measurements, *J. Geophys. Res.*, 78, 2885, 1973.
- Gruntman, M., Energetic neutral atom imaging of space plasmas, *Rev. Sci. Instrum.*, 68, 3617, 1997.
- Henderson, M. G., et al., First energetic neutral atom images from Polar, *Geophys. Res. Lett.*, 24, 1167, 1997.
- Herrero, F. A., and M. Smith, Imager of low energy neutral atoms (ILENA): Imaging neutrals from the magnetosphere at energies below 20 keV, in *Instrumentation for Magnetospheric Imagery*, *Proc. SPIE Int. Soc. Opt. Eng.*, vol. 1744, 32, 1992.
- Horanyi, M., et al., Toward understanding the rate of dust lost from the Martian satellites, *Geophys. Res. Lett.*, 17, 853, 1990.
- Ip, W.-H., On the oxygen corona of Mars, *Icarus*, 76, 135-145, 1988.
- Juhász, A., et al., On the density of the dust halo around Mars, *J. Geophys. Res.*, 98, 1205, 1993.
- Kozyra, J. U., et al., Energetic O⁺ Precipitation, *J. Geophys. Res.*, 87, 2481, 1982.
- Kozyra, J. U., Magnetic storm effects in the inner magnetosphere - The Decay of the Earth's ring current, in *Physics of Space Plasmas*, SPI Conference Proceedings and Reprint Series, No. 12, Scientific Publishers Inc., Cambridge, MA, p. 185, 1992.
- Kozyra, et al., The high altitude energy source for stable auroral red (SAR) arcs, *Rev. of Geophysics*, 35, 2, 155, 1997.
- Krasnopolsky, V. A., and Gladstone, Helium on Mars: EUVE and PHOBOS data and implications for Mars' evolution, *J. Geophys. Res.*, 101, 15,765, 1996.
- Kallio E., An empirical model of the solar wind flow around Mars, *J. Geophys. Res.*, 101, 11,133, 1996.
- Kallio, E., J. G. Luhmann, and S. Barabash, Charge exchange near Mars: The solar wind absorption and energetic neutral atom production, *J. Geophys. Res.* 102, 22,183, 1997.
- Luhmann, J. G. and J. U. Kozyra, Dayside pickup oxygen ion precipitation at Venus and Mars: Spatial distributions, energy deposition and consequences, *J. Geophys. Res.*, 96, 5457, 1991.
- Luhmann, J. G. and L. H. Brace, Near-Mars Space, *Rev. Geophys.* 29, 121, 1991.
- Luhmann, J. G., et al., Evolutionary impact of sputtering of the Martian atmosphere by O⁺ pickup ions, *Geophys. Res. Lett.*, 19, 2151, 1992.
- Lundin, R., et al., First measurements of the ionospheric plasma escape from Mars, *Nature*, 341, 609, 1989.
- Lundin, R., et al., Plasma composition measurements of the Martian magnetosphere morphology, *Geophys. Res. Lett.*, 17, 877, 1990.
- Lundin, R., et al., On the momentum transfer of the solar wind to the Martian topside ionosphere, *Geophys. Res. Lett.* 18, 1059, 1991.
- Lundin, R., et al., ASPERA observations of Martian magnetospheric boundaries, in *Plasma environments of non-magnetic planets*, ed. by T. I. Gombosi, Pergamon Press, p. 311, 1993.
- McKenna-Lawlor, S. M. P., et al., First identification in energetic particles of characteristic plasma boundaries at Mars and account of various energetic particle populations close to the planet, *Planet. Space. Sci.*, 41, 373, 1993.
- Nagy, A. F., and T. Cravens, Hot oxygen atoms in the upper atmospheres of Venus and Mars, *Geophys. Res. Lett.*, 15, 433, 1988.
- Perez-de-Tejada, H., Solar wind erosion of the Mars early atmosphere, *J. Geophys. Res.*, 97, 3159, 1992.
- Roelof, E. C., Energetic neutral atom image of a storm-time ring current, *Geophys. Res. Lett.*, 14, 652, 1987.
- Roelof, E. C., ENA emission from nearly mirroring magnetospheric ions interacting with the exosphere, *Adv. Space Res.*, 20, 361, 1997.
- Vaisberg, O. L., Mars - Plasma environment, in *Physics of Solar Planetary environment*, vol. 2, ed. by D. J. Williams, p. 845, AGU, Washington, D.C., 1976.
- Verigin, M., et al., On the problem of the Martian atmosphere dissipation: PHOBOS 2 TAUS spectrometer results, *J. Geophys. Res.*, 96, 19,315 - 19,320, 1991.
- Zhang, M. H., et al., The ancient oxygen exosphere of Mars: implications for atmospheric evolution, *J. Geophys. Res.*, 98, 10,915, 1993.

ASPERA - 3 Investigators

Barabash, Stanislav

Swedish Institute of Space Physics
Box 812 S-981 28, Kiruna
Sweden
e-mail: stas@irf.se
phone: (+46) 980 79122
fax: (+46) 980 79050

Cerulli-Irelli, Riccardo

Instituto di Fisica
dello Spazio Interplanetario (IFSI)
CNR, Area della Ricerca di Tor Vergata
via del Fosso del Cavaliere, 00133 ROMA
Italy
e-mail: cerulli@ifsi.rm.cnr.it
phone: (+39) 6 4993 4377
fax: (+39) 6 4993 4383

Curtis, Charles

Univ. of Arizona
Department of Physics
1118 East Fourth Street
PAS 557, Tucson, AZ 85721
USA
e-mail: curtis@physics.arizona.edu
phone: (+1) 520 6216770
fax: (+1) 520 6214721

Fedorov, Andrei

Space Research Institute
Profsojuznaya st. 84/32, 117810 Moscow
Russia
e-mail: af@afed.iki.rssi.ru
phone: (+7) 095 333 1467
fax: (+7) 095 3107023

Frahm, Rudy

Southwest Research Institute
Drawer 28510 San Antonio TX 78284
USA
e-mail: rfracm@swri.edu
phone: (+1) 210 522 3855
fax: (+1) 512 647 4326

Gimholt, Joakim

Swedish Institute of Space Physics
Box 812 S-981 28, Kiruna
Sweden
e-mail: jogi@irf.se
phone: (+46) 980 79055
fax: (+46) 980 79050

Grande, Manuel

Rutherford Appleton Laboratory
Chilton, Didcot, Oxfordshire OX11 0QX UK
e-mail: grande@solg2.bnsc.rl.ac.uk
phone: (+44) 1235 446501
fax: (+44) 1235 446509

Hsieh, Ke Chiang

Univ. of Arizona
Department of Physics
1118 East Fourth Street
PAS 565, Tucson, AZ 85721 USA
e-mail: hsieh@physics.arizona.edu
phone: (+1) 520 6216772
fax: (+1) 520 6214721

Kallio, Esa

Finnish Meteorological Institute
Geophysical Research
Box 503, FIN-00101 Helsinki
Finland
e-mail: Esa.Kallio@fmi.fi
phone: (+358) 9 1929 4636
fax: (+358) 9 1929 4603

Koskinen, Hannu

University of Helsinki
Department of Physics
Box 9, FIN-00014
Helsinki University
Finland
e-mail: Hannu.Koskinen@fmi.fi
phone: (+358) 9 191 8256
phone: (+358) 9 1929 4639 (FMI)
fax: (+358) 9 191 8366

Kozyra, Janet

University of Michigan
1411-c Space Research Bldg.
2455 Hayward, Ann Arbor, MI 48109-2143
USA
e-mail: jukozyra@engin.umich.edu
ph: (+1) 734 6473550
fax: (+1) 734 6473083

Krupp, Norbert

Max Planck Institut für Aeronomie
Max Planck Strasse 2
D-37191 Katlenburg-Lindau
Germany
e-mail: Krupp@linmpi.mpg.de
phone: (+49) 5556 979 154
fax: (+49) 5556 979139

Livi, Stefano

Max Planck Institut für Aeronomie
Max Planck Strasse 2
D-37191 Katlenburg-Lindau
Germany
e-mail: livi@linmpi.mpg.de
phone: (+49) 5556 979429
fax: (+49) 5556 979139

Luhmann, Janet

Space Science Laboratory
University of California
Berkeley, CA 94720-7450
USA
e-mail: jgluhman@ssl.berkeley.edu
phone: (+1) 510-642-2545
fax: (+1) 510 643 8302

Lundin, Rickard

Swedish Institute of Space Physics
Box 812 S-981 28, Kiruna
Sweden
e-mail: rickard@irf.se
phone: (+46) 980 79063
fax: +46-980-79050

Norberg, Olle

Swedish Institute of Space Physics
Box 812 S-981 28, Kiruna
Sweden
e-mail: olle@irf.se
phone: (+46) 980 79119
fax: (+46) 980 79050

Orsini, Stefano

Istituto di Fisica
dello Spazio Interplanetario (IFSI)
CNR, Area della Ricerca di Tor Vergata
via del Fosso del Cavaliere 00133 ROMA
Italy
e-mail: orsini@ifsi.rm.cnr.it
phone: (+39) 6 4993 4376
fax: (+39) 6 4993 4383

Roelof, Edmond

Applied Physics Laboratory
The Johns Hopkins University,
Laurel, MD, 20723-6099 USA
e-mail: edmond.roelof@jhuapl.edu
phone: (+1) 240 2285411
fax: (+1) 240 2286670

Sandel, Bill

Lunar and Planetary Laboratory
1040 East Fourth Street, Room 901

University of Arizona
Tucson, AZ 85721 USA
e-mail: sandel@arizona.edu
phone: (+1) 520 6214305
fax: (+1) 520 6218364

Sauvaud, Jean-Andre

CESR/CNRS
9, avenue du colonel Roche
BP 4346, 31028 Toulouse, cedex 4
France
eml: Jean-Andre.Sauvaud@cesr.cnes.fr
phone: 33 5 61 556676
fax: (+33) 5 61 556701

Sharber, James

Southwest Research Institute
Drawer 28510 San Antonio TX 78284
USA
e-mail: jsharber@swri.edu
phone: (+1) 210 522 3853
fax: (+1) 512 647 4326

Williams, Donald

Applied Physics Laboratory
The Johns Hopkins University,
Laurel, MD, 20723-6099 USA
e-mail: djw@aplcomm.jhuapl.edu
phone: (+1) 240 228-5405
fax: (+1) 240 228-6904

Winningham, David

Southwest Research Institute
Drawer 28510 San Antonio TX 78284
USA
e-mail: david@cluster.space.swri.edu
phone: (+1) 512 522 3075
fax: (+1) 512 647 4326

Woch, Joachim

Max Planck Institut für Aeronomie
Max Planck Strasse 2
D-37191 Katlenburg-Lindau
Germany
e-mail: woch@linax1.dnet.gwdg.de
phone: (+49) 5556 979 447
fax: (+49) 5556 979139

Yamauchi, Masatoshi

Swedish Institute of Space Physics
Box 812 S-981 28, Kiruna
Sweden
e-mail: yama@irf.se
phone: (+46) 980 79120
fax: (+46) 980 79050